ISSN 1063-7745, Crystallography Reports, 2006, Vol. 51, No. 6, pp. 908–935. © Pleiades Publishing, Inc., 2006.
Original Russian Text © V.L. Aksenov, M.V. Koval'chuk, A.Yu. Kuz'min, Yu. Purans, S.I. Tyutyunnikov, 2006, published in Kristallografiya, 2006, Vol. 51, No. 6, pp. 971–1000.

DIFFRACTION AND SCATTERING OF IONIZING RADIATIONS

Dedicated to the 50th Anniversary of the Journal

Development of Methods of EXAFS Spectroscopy on Synchrotron Radiation Beams: Review

V. L. Aksenov[a, b], M. V. Koval'chuk[a, c], A. Yu. Kuz'min[d], Yu. Purans[d], and S. I. Tyutyunnikov[b]

[a] *Russian Research Centre Kurchatov Institute, pl. Akademika Kurchatova 1, Moscow, 123182 Russia*
[b] *Joint Institute for Nuclear Research, ul. Zholio-Kyuri 6, Dubna, Moscow oblast, 141980 Russia*
[c] *Shubnikov Institute of Crystallography, Russian Academy of Sciences, Leninskiĭ pr. 59, Moscow, 119333 Russia*
[d] *Institute of Solid-State Physics, Kengaraga Street 8, LV-1063, Riga, Latvia*
e-mail: Sergey.Tiutiunnikov@sunse.jinr.ru

Received April 28, 2006

Abstract—The theoretical fundamentals of extended X-ray absorption fine-structure (EXAFS) spectroscopy are discussed. This method makes it possible to obtain short-range order parameters for multicomponent amorphous and quasicrystalline media with a high accuracy. Methods of analysis of EXAFS spectra with allowance for the effects of multiple scattering are described. Experimental setups implementing EXAFS spectroscopy on synchrotron radiation beams are considered and the requirements on monochromatization of radiation beams are given. A brief description of the energy-dispersive EXAFS spectrometer at the Kurchatov Synchrotron Radiation Source is given. The results of experimental investigations of tungsten and molybdenum oxides and fullerides are reported.

PACS numbers: 78.70.Dm, 61.10.Ht

DOI: 10.1134/S1063774506060022

CONTENTS

INTRODUCTION

In the last 15 years, X-ray absorption spectroscopy (XAS) has found wide application in determination of the local atomic and electronic structures of absorbing centers (atoms) in materials science, physics, chemistry, biology, and geophysics. The rapid progress of XAS is related to the appearance of a large number of synchrotron sources throughout the world and significant achievements in the theory of this method and its practical realization in convenient and easily accessible software packages [1]. XAS makes it possible to obtain information that significantly supplements the results obtained by such experimental methods as X-ray diffraction, neutron diffraction, X-ray photoelectron spectroscopy, and X-ray emission spectroscopy. The main advantages of XAS are its selectivity in the type of a chemical element (and, in some cases, in its location in a material), a circumstance that makes it possible to obtain data on pair and polyatomic distribution functions for the local environment of each element of the material under study; sensitivity to partial densities of free states near the Fermi level; high concentration sensitivity (to 10–100 particles per mole); relatively short times of measuring experimental spectra (from milliseconds to tens of minutes) with the use of synchrotron radiation; and small sample volumes necessary for analysis (generally, amounts lower than 30 mg/cm^2 are sufficient). These advantages make XAS especially promising in the study of crystalline and disordered (amorphous, glassy, liquid, and gaseous) multicomponent materials as well as for in situ investigations of dynamic processes (phase transitions and chemical reactions).

During absorption of X rays with an energy close to the binding energy of electrons, specific features known as absorption edges are observed. A typical X-ray absorption spectrum for the *K* edge of nickel in polycrystalline NiO is shown in Fig. 1. A fine structure can be seen, which extends far beyond the absorption edge and has an oscillating character. For convenience of interpretation, two regions are often distinguished: X-ray absorption near-edge structure (XANES) and extended X-ray absorption fine structure (EXAFS).

It is agreed that the XANES region goes 50–100 eV beyond the absorption edge and is determined by the local density of free states of the absorbing atom and the contributions from scattering of an excited photoelectron from the potentials of several atoms, phenomenon referred to as the multiple scattering effects. In the phenomena EXAFS region, which is located at higher energies, single scattering processes are most often dominant. This region is generally extended 400–2000 eV beyond the edge; the upper limit is determined by the signal-to-noise ratio and/or the presence of another absorption edge. Note that such a division of the X-ray absorption spectrum into two regions is purely conditional and the interval of each region may vary for different compounds. Therefore, the term *X-ray absorption fine structure* (XAFS) is often used in the modern literature for the entire oscillating component beyond the absorption edge.

The fine structure beyond the absorption edge was experimentally observed for the first time 70 years ago [2–8]. However, it took more than 40 years to interpret it. The first theoretical explanation of the XAFS nature (which thereafter was found to be incorrect) was proposed in 1931 [9]. This explanation implied the presence of long-range order in the system. A year later, a theory based on the fundamental role of short-range order was proposed [10]. It explained the XAFS by modulation of the wave function of the final state of a photoelectron upon its scattering from the potentials of neighboring atoms. This approach, developed later in a number of studies [11–15], is the basis of the modern concept of XAFS.

A radical advance in the development of XAS occurred at the beginning of the 1970s, when it was shown in [16] that Fourier transformation of EXAFS oscillations gives a pattern close to the function of radial distribution of atomic density. This argument was in favor of the crystallographic nature of the information present in EXAFS oscillations. In addition, it was shown that spectroscopic measurements in the XANES region in the soft X-ray range (from 300 eV to 10 keV) make it possible to obtain information about unoccupied states near the Fermi level with a good energy resolution [17, 18]. The use of synchrotron radiation (having a continuous spectrum) was a strong impetus for the development of EXAFS spectroscopy and its various applications because the brightness of a synchrotron radiation source exceeds that of an X-ray tube by many orders of magnitude. This circumstance makes it possible to measure EXAFS spectra both at low concentrations of the element under study and for small times (down to several milliseconds) [19].

The first synchrotron radiation sources were developed on the basis of the storage rings VÉPP-3 (Russia, 1971), ADONE (Italy, 1979), ACO (France, 1970), and SPEAR (the United States, 1973) [20]. Currently, synchrotron radiation sources of the third generation are being put into operation—ESRF (France), ALS and

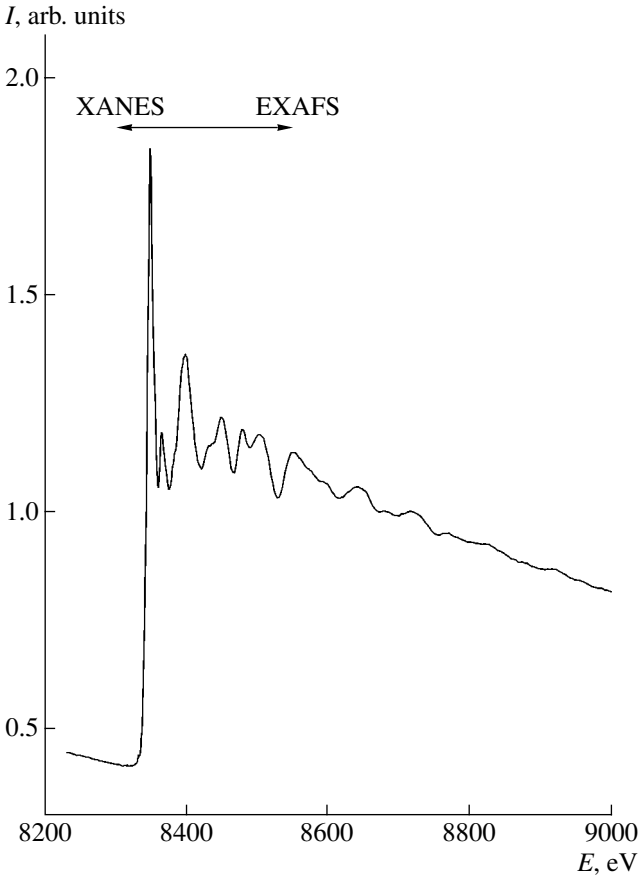

Fig. 1. *K*-edge X-ray absorption spectrum of nickel in NiO [27].

APS (the United States), ELETTRA (Italy), and SPRING8 (Japan)—with a radiation brightness up to $\sim 10^{19}$ $\frac{\text{photons}}{\text{s mm}^2\text{mrad}^2 \times 10^{-3}\frac{\Delta\lambda}{\lambda}}$. On the whole, there are more than 50 operating sources all over the world and more than 10 sources are in the design stage [20]. The use of synchrotron radiation having a high intensity and well-pronounced linear or circular polarization opens unique possibilities for research. In particular, a number of new techniques have been developed in XAS to study atomic and electronic structure (both in bulk and surface layers of different thickness):

(i) fluorescence EXAFS (FEXAFS) spectroscopy;

(ii) methods of surface EXAFS (SEXAFS) spectroscopy based on measuring the Auger electron yield, the total or partial electron photocurrent yields, the photostimulated ion desorption yield, or the total external reflection;

(iii) X-ray excited optical luminescence (XEOL) spectroscopy;

(iv) the method for measuring the circular magnetic X-ray dichroism (CMXD), which can be used to study the magnetic properties of materials [21]; and

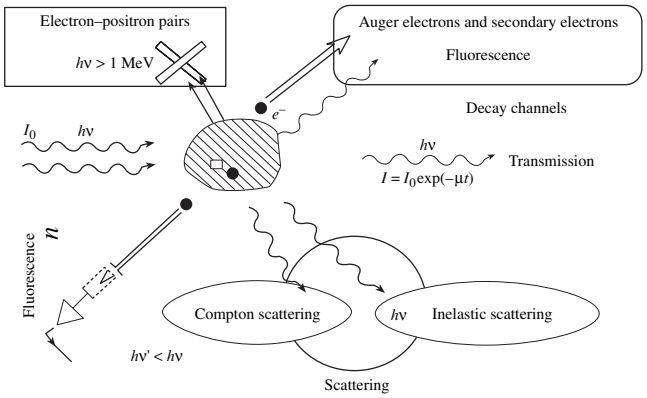

Fig. 2. Elementary events of interaction of X-rays with matter.

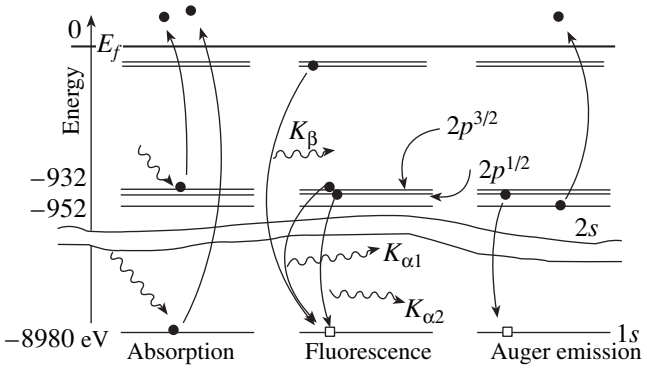

Fig. 3. Energy diagram of the decay of the excited atomic state formed as a result of absorption of an X-ray photon [25].

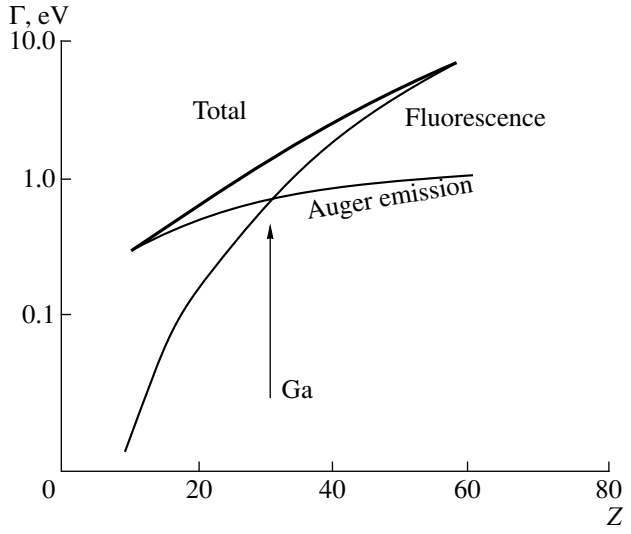

Fig. 4. Dependence of the *K*-shell level width on the nucleus charge [25].

(v) EXAFS spectroscopy based on measuring the intensity of Bragg peaks (diffraction anomalous fine structure (DAFS)).

The main purpose of this review is to give insight into the experimental possibilities of EXAFS spectroscopy in condensed matter physics and to attract the attention of researchers to this promising method, which is being successfully developed in Russia. EXAFS spectrometers operate at the Siberian Synchrotron Radiation Center and at the Russian Research Centre Kurchatov Institute. A new energy-dispersive EXAFS spectrometer has been put into operation at the Kurchatov Synchrotron Radiation Source.

1. FUNDAMENTALS OF XAS

XAS is based on the interaction of incident radiation with a solid. The main elementary processes occurring during transmission of radiation through a material are shown in Fig. 2. These processes lead to the circumstance that the intensity of the X rays transmitted through a sample weakens according to the exponential law $I_x = I_0\exp\{-\mu x\}$. The absorption coefficient μ is determined by different elementary processes: photoelectron absorption, Compton scattering, elastic scattering, and generation of pairs [22].

For the range of X-ray photon energies $\hbar\omega$ below 100 keV, photoelectron absorption has the maximum cross section. This process is accompanied by the generation of a photoelectron with an energy $E = \hbar\omega - E_0$, where E_0 is the binding energy of electrons in absorbing atoms. At energies of incident photons in the range 300–30 000 eV, the photoelectron energy E is 1–1000 eV.

During the absorption of an X-ray photon by an atom, excitation occurs, which is removed through either discrete photon emission (fluorescence) or emission of Auger electrons from the atom. Auger electrons have certain energies corresponding to the energy levels of the atomic system. Figure 3 shows a diagram of the decay of an excited state of an atom. The probabilities of different decay channels (Auger process and fluorescence) depend on the nucleus charge and are shown in Fig. 4 in terms of level width units (in eV) [23]. The level widths determine the experimental resolution that is necessary for level separation.

The cross section σ of absorption of photons by an atom is determined in the dipole approximation by the transition probability $\sigma = 2\pi/\hbar\sum\langle f|W|i\rangle^2\delta(E_\mathrm{f} - E_\mathrm{i} - \hbar\omega)$, where W is the operator of the dipole transition under the action of incident electromagnetic radiation ($W = e\mathbf{r}\cdot\mathbf{E}$, where $\mathbf{E}$ is the electric field strength in the incident wave and $e\mathbf{r}$ is the atomic dipole moment [24]) and E_f and E_i are the energies of the atom in the final and initial states, respectively.

If we introduce the polarization vector $\boldsymbol{\varepsilon} = \mathbf{E}/|E|$ of incident radiation, the absorption cross section for

the dipole and quadrupole transitions will take the following forms [24]:

$$\sigma(\omega) = 4\pi\alpha^2\hbar\omega\sum\langle f|\boldsymbol{\varepsilon}\mathbf{r}|i\rangle\delta(E_f - E_i - \hbar\omega), \quad (1)$$

the dipole approximation, and

$$\sigma(\omega) = 4\pi\alpha^2\frac{1}{4}\hbar\omega\sum\langle f|(\boldsymbol{\varepsilon}\mathbf{r})(\mathbf{k}\mathbf{r})|i\rangle^2\delta(E_f - E_i - \hbar\omega), \quad (2)$$

the quadrupole approximation.

Taking into account (1) and (2), we obtain the following: (i) selectivity in excitation, determined by the photon energy $\hbar\omega$; (ii) dichroism, determined by the dipole transition operator $\boldsymbol{\varepsilon}\mathbf{r}$ with the components $\boldsymbol{\varepsilon}\times\mathbf{z}$ or $(\varepsilon_x - i\varepsilon_y)(\varepsilon_x + i\varepsilon_y)$; (iii) the selection rules $\Delta l = \pm 1$; and (iv) the effect of relaxation of the final state on the total transition probability.

In the case of excitation of neutral atoms, which do not interact with each other, the energy dependence of the excitation cross section is determined by the selection rule with respect to the orbital momentum $\Delta l = \pm 1$ and the energy conservation law $\delta(E_f - E_i - \hbar\omega)$. Figure 5 shows the dependence of the photoabsorption cross section of neon on the energy of X-ray photons for which the function of the initial and final states are, respectively, $|i\rangle = |1s^2 2s^2 2p^6\rangle$ and $|f\rangle = |1s' \ldots np^1\rangle$ [25].

As can be seen in Fig. 5, the absorption cross section is completely determined by the energy levels of an individual atom.

In the case of absorption of a photon by an atom surrounded with other atoms, the pattern of interaction becomes significantly complicated.

In Fig. 6, schematic diagrams illustrate the process of photon absorption by an atom in a solid. At photon energies exceeding the electron binding energy in an atom, an electron with an energy E and a wave vector $\mathbf{k}$ becomes excited. This electron is scattered by the potentials of the neighboring atoms (including the potential of the absorbing atom itself). At low photoelectron energies and, accordingly, large wavelengths, which are comparable with the interatomic distances R_0 in the crystal lattice (a situation corresponding to the XANES region), the contribution of multiple scattering generally significantly exceeds that of single scattering events. At high photoelectron energies, the de Broglie wavelength is very small, and the processes of single scattering generally dominate.

XANES spectra contain information about the electronic state of an absorbing atom (its valence and density of free states) [25, 26]. Figure 7 shows the XANES spectra [25] measured at different angles for pure metals, powders, and single crystals. The angular dependence of these spectra reflects the fact that polarized synchrotron radiation effectively interacts with electrons of different configurations: at $\theta = 0°$, photons in La_2CuO_4 single crystals interact with electrons in the *ab* plane, which are bound through the 4*px*, *y* orbitals.

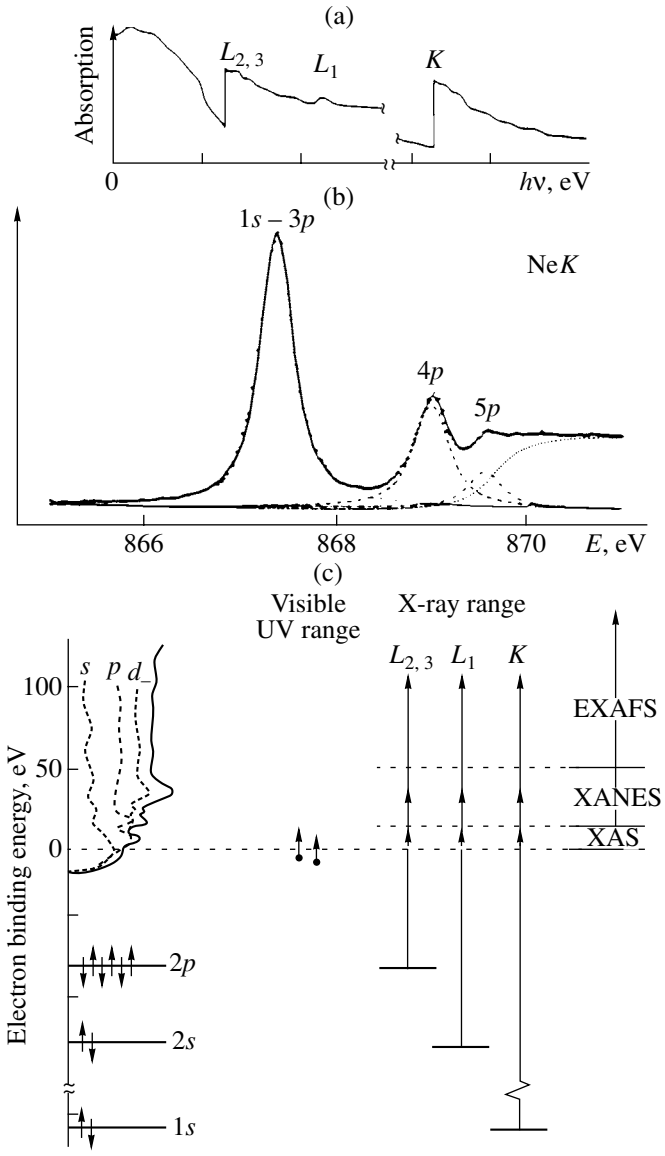

Fig. 5. (a) Energy-level diagram of neon and (b, c) the dependence of the photoabsorption cross section of neon on the X-ray photon energy (a) in a wide spectral range and (b) near the *K* edge.

The *M* and *N* peaks correspond to this process. For $\theta \geq 54°$, interaction with the 4*pz* electrons (*BE* transitions) manifests itself.

Figures 8a and 8b show the XANES spectra of $La_{1-x}Sr_xCoO_3$ solid solutions (x = 0–0.5) [26]. Four features can be singled out near the absorption edge. They can be interpreted as transitions of a photoelectron excited from the 1*s* level of cobalt to bound states and the processes of its scattering by the local environment. The specific feature located before the fundamental absorption edge corresponds to the $1s \longrightarrow 3d$ transition. Note that the 3*d* states are split by the octahedral crystal field into the t_{2g} and e_g sublevels. The further splitting of the 3*d* level is related to the presence of

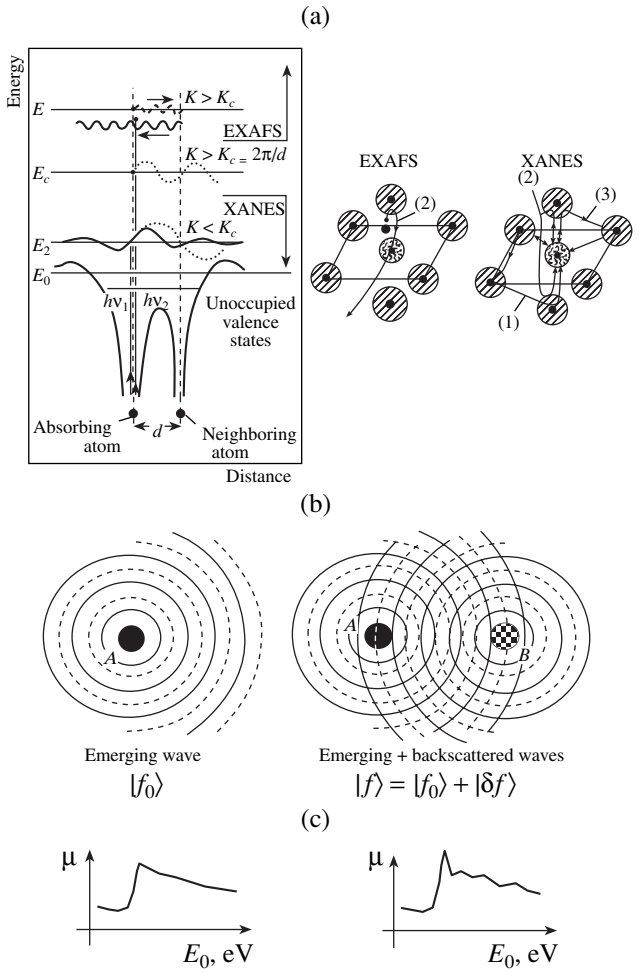

Fig. 6. Scheme of interaction of a photoelectron with the atoms of the nearest environment (*A* is the atom absorbing an X-ray photon and *B* is a neighboring atom): (a) the energy-level diagram of electrons in a crystal lattice at different excitation energies corresponding to single-scattering (EXAFS) and multiple scattering (XANES) processes, (b) emerging wave corresponding to a free electron and the interference between the emerging and scattered waves, and (c) the energy dependence of X-ray absorption in the absence of scattering from neighboring atoms and in the presence of scattering.

Jahn–Teller distortions as well. The replacement of La^{3+} with Sr^{2+} in $La_{1-x}Sr_xCoO_3$ leads to a change in the XANES signal above 7715 eV, which is related to the modification of the local structure of Co ions. In addition, a red shift of the pre-edge peak by approximately 1 eV is observed (Fig. 8b). This result is nontrivial because the replacement of Co^{3+} with Co^{4+} with an increase in the strontium content should formally lead to a shift in the opposite direction owing to the increase in the electron binding energy with an increase in the effective positive charge of the atomic core. Therefore, the effect observed can be related to a change in the screening of an excited electron by other electrons located in the $3d(t_{2g})$ state.

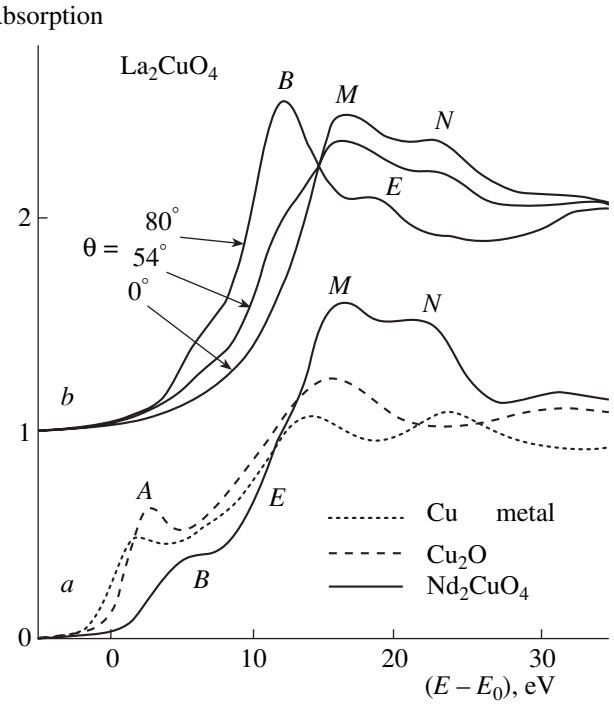

Fig. 7. XANES spectra measured at different angles of incidence of X-rays on the crystal surface [25].

The EXAFS model is based on the description of the transition probability from the initial atomic state to the final excited state, which is described by the wave function of a free electron. This transition occurs as a result of absorption of a photon with an energy $\hbar\omega$. According to the scattering theory, if an absorbing atom has a neighboring atom, the electron is scattered from this neighbor. As a result, two waves (initial and scattered) arise and interfere with each other. The phase difference is determined by the interatomic distance and the electron wave vector **k**. Figure 6 schematically shows all main processes occurring during absorption of a photon with an energy $\hbar\omega$ exceeding the threshold energy E_0 of photoelectron emission in the solid. As mentioned above, the interaction cross section of a photon and an atom is determined by expression (1):

$$\sigma = |M|^2 \sum \int d^3x \left|\varphi_{i\text{rem}}(x)\boldsymbol{\varepsilon}\mathbf{r}\varphi_{i_f}\right|^2 \times \delta(E_i - E_{f,R} - \hbar\omega + \varepsilon_f), \quad (3)$$

where $M = \langle \Psi_i^{N-1} | \Psi_{f,R}^{N-1} \rangle$ is the monopole matrix element of the transition from the initial state of a system composed of $N - 1$ electrons, excluding the excited electron with the energy ε_f to the states with completely relaxed $N - 1$ electrons.

Calculation of the wave function of the final state of an electron moving in the potential of remaining $N - 1$ electrons in the ground state takes into account the interaction of this electron with the neighboring atoms

with allowance for the vacancies formed in the framework.

In the single-scattering approximation, the wave function has the general form

$$\varphi_{\varepsilon_f}(x) = \varphi_\varepsilon^{abs}(x) + \sum_{Rj} \varphi_\varepsilon^{scat}(x - R_j), \quad (4)$$

where $\varphi_\varepsilon^{abs}$ is the wave function of a free electron generated as a result of the absorption of a photon and $\varphi_\varepsilon^{scat}(x - R_j)$ is the wave function of the electron scattered by an atom located at a distance R_j from the atom absorbing the photon. Substituting (4) into expression (3), we obtain the photon–atom interaction cross section with allowance for the nearest environment:

$$\sigma(\omega) = \sigma^{abs}(\omega)(1 + \chi(\omega)), \quad (5)$$

where $\sigma^{abs}(\omega)$ is the classical scattering cross section of a photon and $\chi(\omega)$ is the EXAFS modulation of the atomic cross section by the nearest environment:

$$\chi(\omega) = \frac{1}{\sigma^{abs}(\omega)} \sum_{Rj} 2R_j \int d^3x \varphi^*_{irem}(x) \boldsymbol{\varepsilon} \mathbf{x} \varphi^{abs}_{\varepsilon, lm} \times \int d^3x' \varphi^*_{irem}(x') \boldsymbol{\varepsilon} \mathbf{x} \varphi^{scat}_{\varepsilon l m R_j}(x'). \quad (6)$$

Here, $\varphi^{abs}_{\varepsilon lm}$ is the wave function corresponding to the electron with an energy ε and momentum l that has escaped from the atom and $\varphi^{scat}_{\varepsilon lm R_j}$ is the scattered wave from the neighboring atom located at the point R_j. The quantum numbers for the emerging wave are determined by the selection rules for the dipole transition with $l = 1$ for the k and l absorption.

In the EXAFS region, where the photoelectron wave vector $\mathbf{k}_e$ exceeds the wave vector $k_d = \frac{2\pi}{d}$ corresponding to the first Brillouin zone, $k_e \geq k_d$ (Fig. 6), the wave function of the scattered wave at the distance $|x - R_j|$ from the scattering atom can be written in the asymptotic form:

$$\varphi^{scat}_{\varepsilon lm}(x) = \varphi^{abs}_{\varepsilon lm}(R_j) f(\Omega_k) e^{i|k|x} e^{-\mu(|R_j| + |x|)} \frac{1}{|x|} = Y_{lm}(\Omega_{R_j}) e^{i(kR_j + \delta_l)} f(\Omega_k) e^{i|k|x} e^{-\mu(|R_j| + |x|)} \frac{1}{|k| R_j |x|}, \quad (7)$$

where δ_1 is the phase shift of the wave at the absorbing atom, Ω_k is the solid scattering angle with respect to the scattering atom, $\Omega_{R_j}(\theta, \varphi)$ is the angle with respect to the straight line connecting the absorbing and scattering atoms, and $f(\Omega_k)$ is the scattering length for the angle Ω_k.

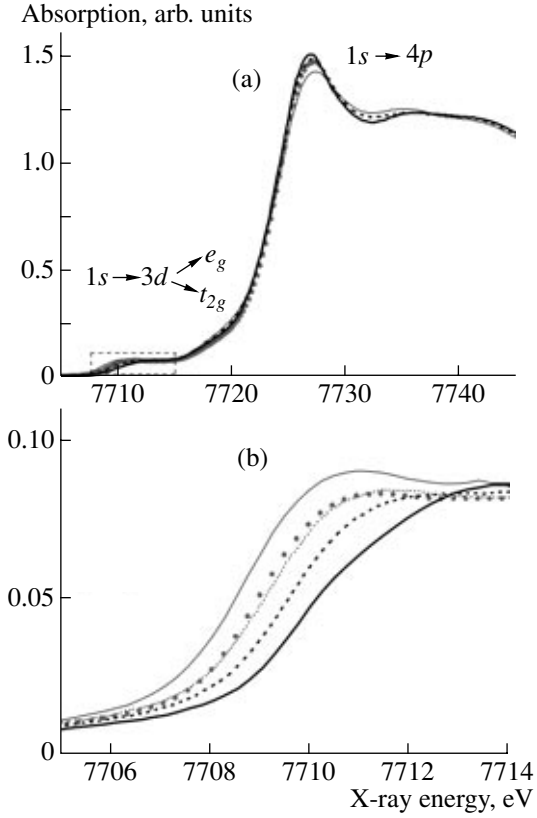

Fig. 8. *K*-edge XANES spectra of cobalt in $La_{1-x}Sr_xCoO_3$ ($x = 0.0$–0.5): (—) $x = 0.0$, (- - -) $x = 0.2$, (···) $x = 0.3$, (•) FIT, (—) $x = 0.5$.

Calculation of the matrix element $\chi(\omega)$ for the distribution in $\{R_j\}$ gives

$$\chi(\omega(\{R_j\})) = \sum_j \frac{|\boldsymbol{\varepsilon} \mathbf{R}_j|}{k|R_j|^2} \mathrm{Im}\{f(\pi) e^{2ik|R_j|} e^{2i\delta_e}\} e^{-2\mu R_j}. \quad (8)$$

Here, $f(\pi) = \sum_{e'} \frac{e^{2i\delta_{e'}} - 1}{2ik} (2l' + 1)(-1)^{l'}$ is the backscattering amplitude (the exponential $e^{-\mu(|R_j| + |x|)}$ determines the mean free path of an electron in the material).

Since neighboring atoms execute thermal vibrations in a solid, the expression for $\chi(\omega, \{R_j\})$ should be averaged over the vibration amplitudes. The averaged expression is given by the $g(R_j)$ distribution:

$$\bar{\chi}(\omega) = \sum_j \int d^3 R_j g(R_j) \chi(\omega; \{R_j\}). \quad (9)$$

For a single crystal, this averaging depends on the relative direction between the polarization vector $\bar{\varepsilon}$ of the incident wave and the crystal axis. For a polycrystalline sample, averaging is performed over all direc-

tions and only the magnitude of variations in $|R|$ is of importance in this case.

The simplest approximation in $\{R_j\}$ is the Gaussian approximation with a dispersion σ^2. The averaged form of the EXAFS factor $\chi(\omega)$ is

$$\bar{\chi}(\omega) = \sum_j \frac{f(\pi)}{k|\bar{R}_j|^2}\sin(2|k|R_j + \bar{\alpha}(k))e^{-k^2\sigma^2}e^{-2\mu R_j}, \quad (10)$$

where the phase shift $\alpha(k)$ is temperature-dependent as well:

$$\alpha_j(\bar{k}) = \left(2\delta_e + \arg f(\pi) - \frac{2k\sigma^2}{R_j} - 2k\mu\sigma^2\right). \quad (11)$$

The factor $e^{-k^2\sigma^2}$ in (10), known as the Debye–Waller factor, takes into account the contribution of the mean-square deviation of the interatomic distance from the mean value for thermal vibrations. It should be noted that the parameter σ differs from the mean-square atomic displacement that is used in the Bragg scattering correction: the latter determines the displacement of an atom with respect to its equilibrium position, whereas the parameter σ in EXAFS spectroscopy characterizes the change in the absorber–scatterer distance R_j.

The phase shift δ_e caused by the central atom depends on the Coulomb potential of the atom, which is determined by the effective ion charge Z_{eff} [24]: $\delta_e = \delta_e^0 + z_{\text{eff}}^0\log(R_j/a_B)/a_B k$, where a_B is the Bohr radius.

The EXAFS formula, with allowance for the fact that the atoms of the nearest environment are described by the pair correlation function $g_j(r)$ (r is the distance between the absorbing and probe atoms), can be written as

$$\chi(k) = \sum_j \frac{f_j(\pi k)}{k} \times \int_0^\infty dr g_j(r)\sin(2kr_j + \alpha_j(k)e^{-k^2\sigma^2}e^{-2\mu(k)r_j}. \quad (12)$$

When this formula is used, one must take into account two main factors that depend strongly on the compound under consideration: (i) the errors related to the neglect of the effects of multiple scattering of an excited electron from atomic potentials and (ii) the degree of coordination disordering, which is determined by the nature of the $g_j(r)$ distribution.

For a discrete distribution of scattering atoms, the EXAFS distribution function $\chi(k)$ has the form

$$\chi(k) = \sum A_j(k)\sin(2kR_j + \bar{\alpha}_j(k)),$$
$$A_j(k) = \frac{N_j}{kR_j^2}F_j(k)e^{-2k^2\sigma^2}. \quad (13)$$

Here, N_j is the number of atoms in the jth coordination sphere; R_j is the distance to the jth coordination sphere; and $F_j(k) = f(k)e^{-2R_j/\lambda}$, where λ is the electron mean free path.

The scattering phase is given by the expression $\bar{\alpha}_j(k) = 2kR_j + \delta_j(k) + \Theta_j(k)$, where $\delta_j(k)$ is the phase shift determined by the charge of a scattering atom and Θ_j is the phase shift resulting from the complex value of the amplitude $f_j(k, \pi) = |f_j(k, \pi)|\exp\{i\Theta_j(k)\}$ of electron backscattering. The results of the calculation of the amplitude and phase were reported in [27].

Fourier transformation of the EXAFS function $\chi(k)$ makes it possible to calculate the quasi-distribution of the density $F(R)$ in real space: $F(R) = \frac{1}{2\pi}\int_{k_{\min}}^{k_{\max}} W(k)\chi(k)e^{2ikR}dk$, where $k_{\min}$ and $k_{\max}$ are, respectively, the minimum and maximum values of the photoelectron momentum $k = \sqrt{\frac{2m}{h^2}(E - E_0)}$, which is determined by the incident photon energy E and the threshold energy E_0 of photoemission from the corresponding level of the absorbing atom. The window function $W(k)$ ($W(k) \longrightarrow 0$ at $k \longrightarrow \pm\infty$) is used to extend the integration limits to $k \longrightarrow \pm\infty$, a procedure that is necessary for correct calculation of Fourier transforms.

Figure 9 shows the EXAFS functions $\chi(k)$ measured at the L_3 edge of rhenium in polycrystalline ReO_3 at different temperatures [27, 28]. Their Fourier transforms $F(r)$ are shown in Fig. 10, where one can clearly see the peaks corresponding to the coordination spheres

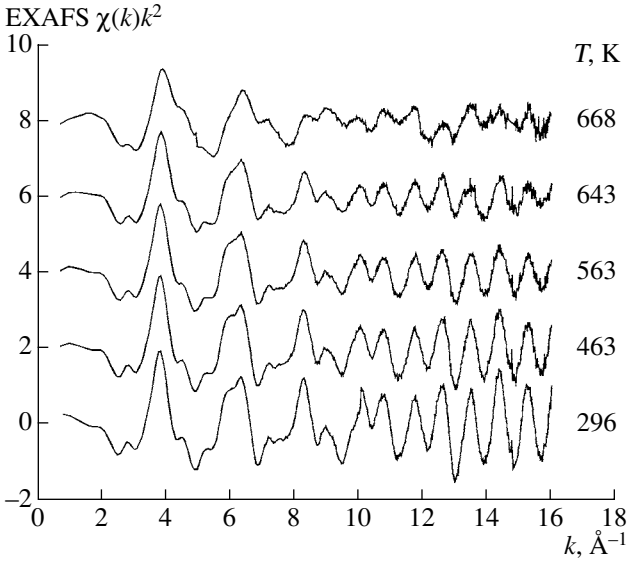

Fig. 9. Temperature dependence of the L_3-edge EXAFS spectra $\chi(k)k^2$ of rhenium in ReO_3 [28].

around the central rhenium atom. Note the fundamental difference between the Fourier transform of the EXAFS function $F(r)$ and the true pair correlation function $g(r)$ (see (10)): the positions and shapes of peaks of the function $F(r)$ are always distorted by the presence of the phase shift $\alpha(k)$ and the amplitude modulation $f(k)$.

2. METHODS FOR ANALYSIS OF EXAFS SPECTRA

As mentioned above, the EXAFS region, which has an oscillating character and is located beyond the absorption edge of an atom, contains information about the local atomic structure. The energy range in which EXAFS oscillations are observed is generally about 400–2000 eV; it is limited by the experimental signal noise and/or the presence of other absorption edges. The general approach to analysis of EXAFS spectra, which has been developed over the last two decades [29–31], implies effective use of modern computers for carrying out high-speed calculations and graphical representation of results in the interactive mode. Below, we will give a brief description of the procedure of processing EXAFS spectra via the EXAFS Data Analysis (EDA) software package, which was developed at the Institute of Solid-State Physics (Riga, Latvia) by Purans in 1988–1998 [32–34].

The EDA software package was designed for use on IBM PC-AT compatible MS-DOS-based computers. The package (version 5.1) consists of eight interactive programs (EDAFORM, EDAXANES, EDAEES, EDAFT, EDAFIT, EDARDF, FTEST, and EDAPLOT), which completely implement both the standard procedure of treatment and calculation of EXAFS spectra [29–31] and some original approaches used in selection and simulation of the EXAFS component [32–34]. The package has an open architecture, thus allowing its easy expansion. The scheme of analysis of EXAFS spectra implemented in the EDA software package is shown in Fig. 11.

The EDAFORM program is used to calculate the X-ray absorption coefficient $\mu(E)$ from the known, experimentally measured X-ray intensities before ($I_0(E)$) and after ($I(E)$) interaction with a sample. When the most widespread measurement technique (in transmission) is used, $I_0(E)$ and $I(E)$ correspond to the intensities of the radiations incident on the sample and transmitted through it, while the absorption coefficient of the sample with a thickness x is determined by the expression $\mu(E) = (1/x)\ln[I_0(E)/I(E)]$.

The shape of the absorption coefficient in the near-edge (XANES) region is often of practical interest. This part of a spectrum is determined to a great extent by the local electronic structure. Analysis of this spectral region remains a difficult problem requiring the use of special approaches (for example, the full multiple scattering (FMS) theory or quantum-mechanical cluster (or zone) calculations [30, 31, 35]). Their consideration is beyond the scope of this paper. The possibility of simulating XANES spectra is absent in the EDA software package; however, the EDAXANES program allows one to single out the absorption coefficient $\mu(E)$ in the near-edge region and perform its differential analysis, i.e., calculate the first ($d\mu(E)/dE$) and second ($d^2\mu(E)/dE^2$) derivatives. This possibility significantly simplifies the qualitative analysis of XANES spectra and determination of the exact position of the absorption edge, which is often used as a reference point on the photoelectron kinetic energy scale in EXAFS spectra [29–31].

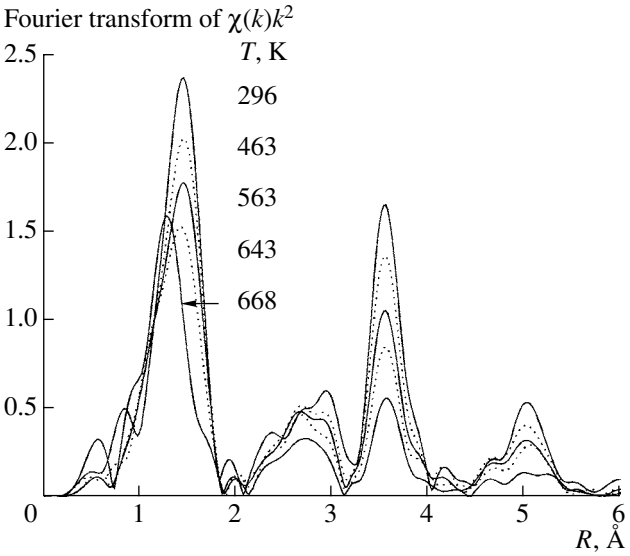

Fig. 10. Temperature dependence of the Fourier transformed L_3-edge EXAFS spectra $\chi(k)k^2$ of rhenium in ReO_3 [28].

The next step in the analysis of an X-ray absorption spectrum is related to selection of the EXAFS component $\chi(k)$, which is determined by the expression [29–31]

$$\chi(k) = (\mu(k) - \mu_0(k) - \mu_b(k))/\mu_0(k),$$

where $\mu_b(k)$ is the absorption coefficient containing contributions of all processes except for the photoionization of the atomic shell under study, $\mu_0(k)$ is the absorption coefficient that would be observed if the absorbing atom had no neighbors, $k = [(2m_e/\hbar^2)(\hbar\omega - E_0)]^{1/2}$ is the modulus of the photoelectron wave vector, m_e is the electron mass, E is the energy of incident X-ray photons, and E_0 is the ionization potential in the case of absorption of an X-ray photon.

Note that currently there are several programs allowing one to perform ab initio simulation of absorption spectra without selection of an EXAFS signal: EXCURVE [36, 37], FEFF [38–41], and GNXAS [42–45]. However, in many practical cases, for example, when preliminary information about the structure of a compound is completely or partially absent or an

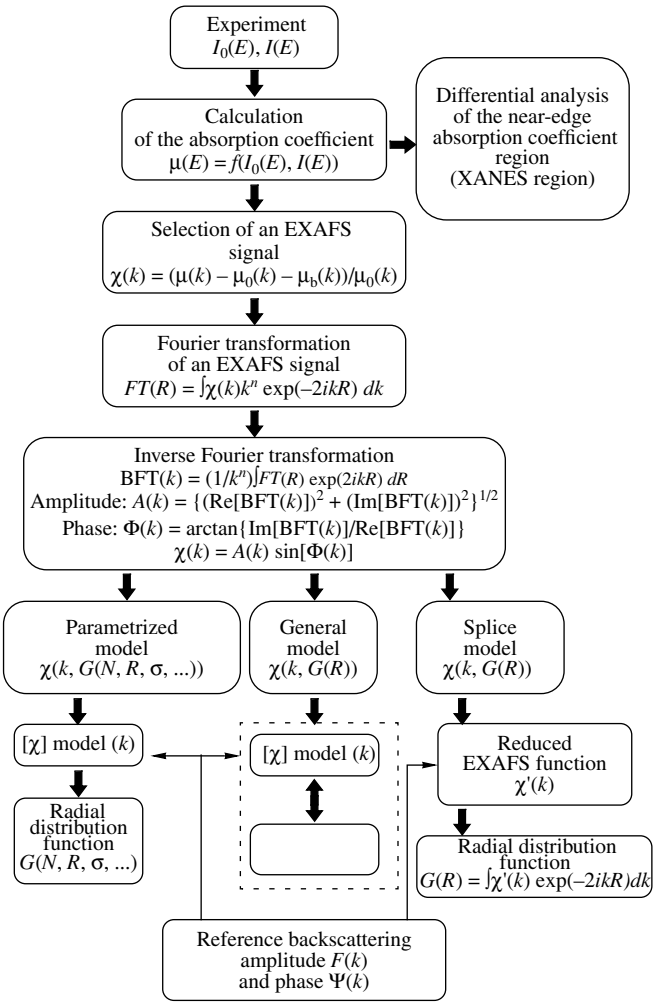

Fig. 11. Scheme of analysis of EXAFS spectra with the use of the EDA software package [32–34].

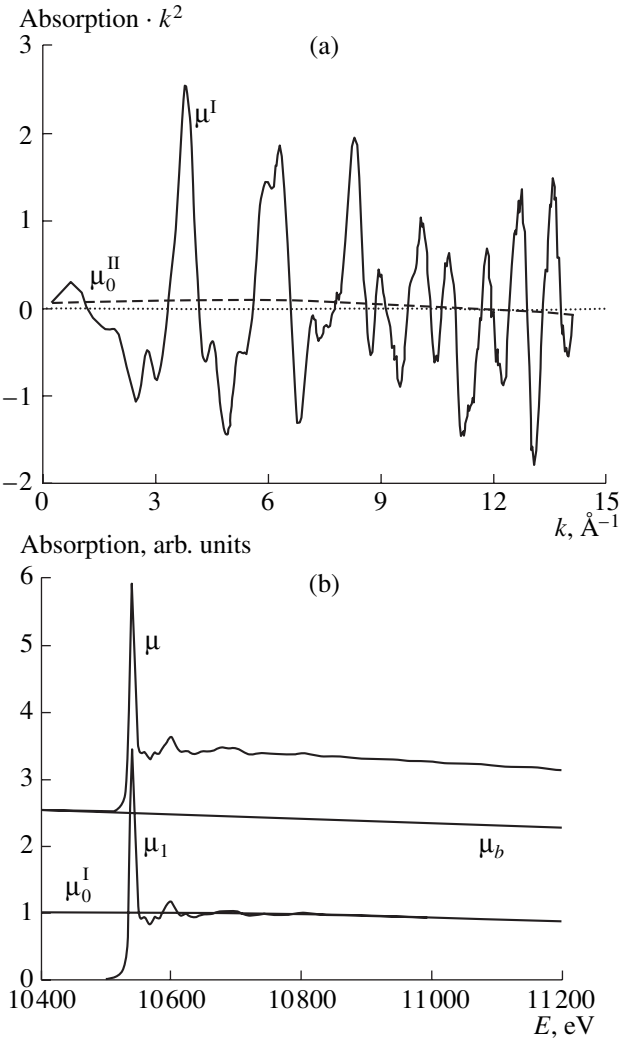

Fig. 12. (a) Function $\mu^I = \mu_1 - \mu_0^I$ translated to the k space and multiplied by the coefficient k^n ($n = 1$) and the function μ_0^{II}, which is the second correction to μ_0. (b) The experimental L_{III} X-ray absorption spectrum of rhenium in ReO_3 before (μ) and after (μ_1) subtraction of the contribution μ_b and the function μ_0^I (the first-order approximation for μ_0).

experimental signal is partially distorted, it is fairly difficult to use the above-mentioned programs. Therefore, in most studies, the EXAFS component is selected and analyzed separately. This approach simplifies the general problem significantly. In the EDA software package, selection of an EXAFS signal $\chi(k)$ is implemented within the EDAEES program by an original technique [32, 34], whose specific feature consists in determining $\mu_0(k)$ via a step-by-step procedure (see below). The criterion for correct determination of the function $\mu_0(k)$ is the absence of any contributions in the EXAFS signal $\chi(k)$ except for oscillations of structural origin. Therefore, the function $\mu_0(k)$ is sometimes referred to as the zero line of an EXAFS signal, i.e., the line with respect to which the oscillating fine structure is located. It should be emphasized that an error in determining $\mu_0(k)$ may lead to significant distortions of the EXAFS signal from the atoms of the first coordination sphere and, thus, to errors in the values of structural parameters.

First, the absorption coefficient $\mu_b(E)$ is approximated by the modified Victorin polynomial $\mu_b(E) = A + B/E^3$, in which the parameters A and B are determined by the least-squares method from the pre-edge part of the experimental absorption coefficient $\mu(E)$. Then, $\mu_b(E)$ is extrapolated to the entire range and is subtracted from $\mu(E)$ (Fig. 12). The obtained function $\mu_1(E) = \mu(E) - \mu_b(E)$ is used in the first stage of determination of the function μ_0, which is approximated by the m_1-order polynomial $\mu_0^I(E)$ (generally, the value of m_1 is chosen in the range from 1 to 4) and subtracted from $\mu_1(E)$ (Fig. 12). The new function $\mu^I(E) = \mu_1(E) - \mu_0^I(E)$ is

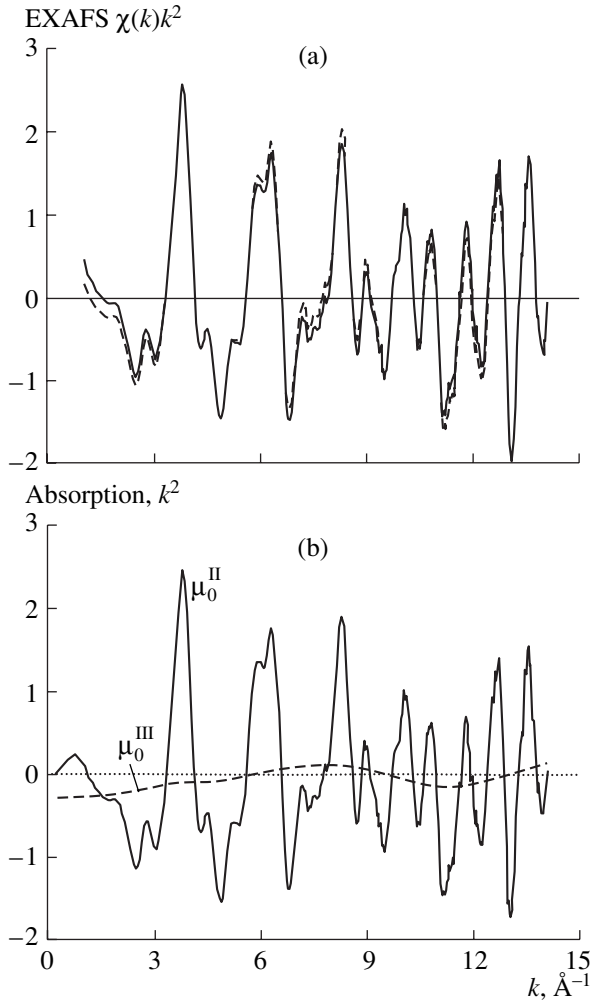

Fig. 13. (a) Third stage in determination of the zero line $\mu_0(k)$: the functions $\mu^{II} = \mu^I - \mu_0^{II}$ and μ_0^{III}; the latter is found via a cubic smoothing spline and is the third correction to μ_0. (b) EXAFS signals calculated from the formulas $\chi(k) = (\mu(k) - \mu_0(k) - \mu_b(k))/\mu_0(k)$ (solid line) and $\chi(k) = (\mu(k) - \mu_0^I(k) - \mu_b(k))/\mu_0^I(k)$ (dashed line).

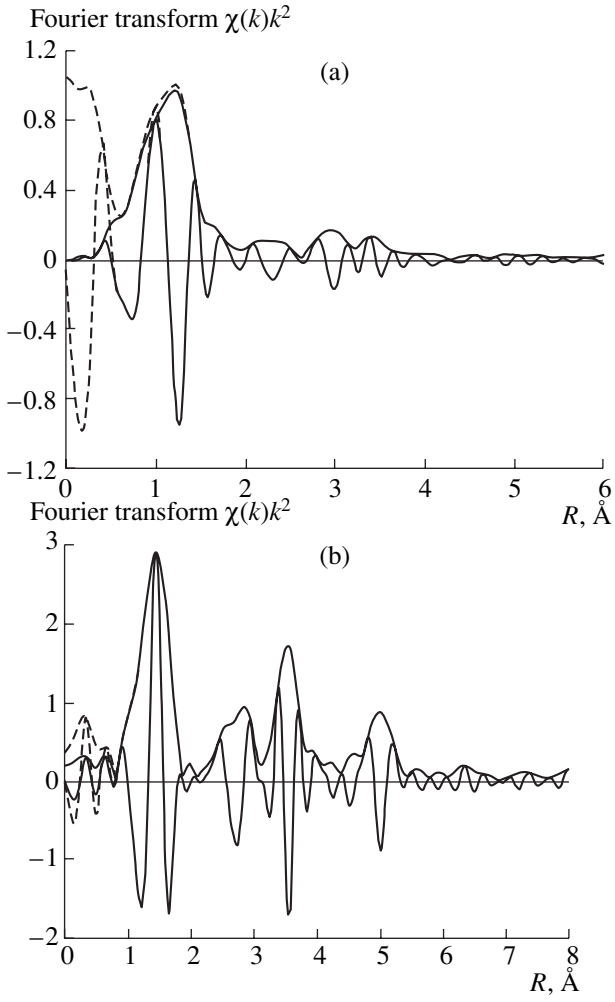

Fig. 14. Fourier transforms of EXAFS signals (a) the L_{III} edge of rhenium in ReO_3 and (b) the K edge of molybdenum in an MoO_3 amorphous film. The EXAFS signals were selected by the three-stage technique described in the text ($\mu_0 = \mu_0^I + \mu_0^{II} + \mu_0^{III}$, the solid line) and the standard technique ($\mu_0 = \mu_0^I$, dashed line).

translated to the k space and multiplied by the coefficient k^n (the value of n is chosen to be equal or larger than the value that is planned to be used in further Fourier analysis and/or simulation; generally, $n = 1$, 2, or 3). In the second stage, the function $\mu_0^{II}(k)$ is sought. This function is set by the m_2-order polynomial (generally, the value of m_2 is chosen in the range from 0 to 9) and is a zero line of $\mu^I(k)$. This operation makes it possible to correct rough errors in the behavior of $\mu^I(E)$ at its translation to the k space and multiplication by the coefficient k^n. Thus, the basic concept of the first two stages consists in obtainment of the function $\mu^{II}(k) = \mu^I(k) - \mu_0^{II}(k)$, which sufficiently well oscillates around zero. The third stage consists in determining the zero line $\mu_0^{III}(k)$ of the function $\mu^{II}(k)$ via a cubic smoothing spline (Fig. 13). This spline makes it possible to compensate for all remaining zero-line errors. As a result, the desired function μ_0 is equal to the sum of μ_0^I, μ_0^{II}, and μ_0^{III}. The effect of the corrections μ_0^{II} and μ_0^{III} on an EXAFS signal is shown in Fig. 13b. This effect is especially pronounced in the Fourier transforms of EXAFS signals (Fig. 14): errors in determining the function μ_0 lead to the appearance of a peak at small distances ($R < 1$ Å), which can distort the signal of the first coordination sphere (the main peak near 1.4 Å).

In most practical cases, the selected EXAFS signal was subjected to Fourier filtration (i.e., direct and inverse Fourier transformation in specified intervals in

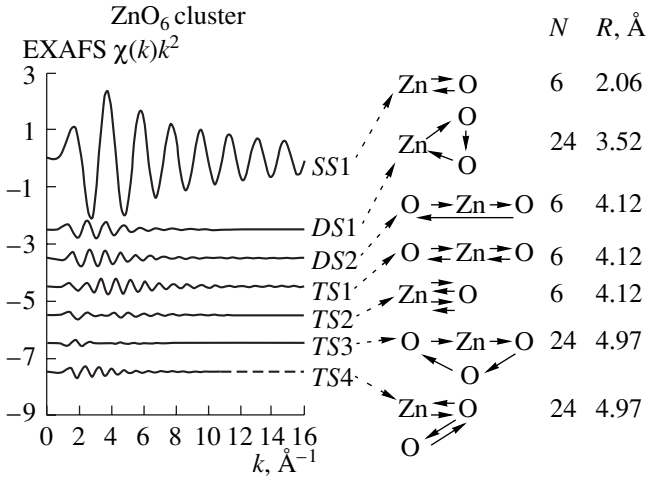

Fig. 15. Calculation of the effects of multiple scattering in the octahedral ZnO_6 cluster; N is the number of identical scattering paths and R is the half path length.

the k and R spaces) to select the contributions of individual coordination spheres. This procedure simplifies EXAFS simulation significantly. In the EDA software package, the procedure of Fourier filtration is implemented in the EDAFT program [34]. To avoid distortion of an EXAFS signal (related to its boundedness in the k space) during Fourier transformation, the window function $W(k)$ is used in order to smooth the cut-off shape of EXAFS oscillations at the smallest and largest values of the wave vector **k**. Several types of window functions $W(k)$ are applied in practice: rectangular, Hemming, Gauss, Kaiser–Bessel, and other functions [29–34]. Experience shows that the Gauss and Kaiser–Bessel window functions introduce the smallest distortions into the Fourier transformation [34]. Note that, in the case of inverse Fourier transformation, along with the EXAFS component of $\chi(k)$, its complete amplitude $A(k)$ and phase $\Phi(k)$ are calculated as well (Fig. 11). These parameters can be used to calculate the backscattering amplitude $F(k)$ and phase $\Psi(k)$ from the known structural parameters or to determine relative changes in the latter from comparison of the phases and the amplitude ratio [29–31].

The shape of the Fourier transform of an EXAFS signal (Fig. 14) resembles the pair radial distribution function of atoms. This resemblance sometimes leads to incorrect interpretation of this signal. The fundamental difference between a Fourier transform and a radial distribution function consists in the following. First, a Fourier transform contains information about both pair and polyatomic distribution functions [43, 44, 46, 47]. Second, the position of peaks in a Fourier transform does not correspond to actual interatomic distances as a result of the phase shift $\Psi(k)$ caused by backscattering of a photoelectron from atoms [29–31]. Third, the shape of the peaks is distorted owing to the contribution of the nonlinear backscattering amplitude $F(k)$ [29–31]. Moreover, each peak does not always correspond to a certain group of atoms. For example, in the case of heavy elements, the complex shapes of the backscattering amplitude and phase lead to the appearance of a two-humped peak in the Fourier transform with the hump amplitudes depending strongly on the Fourier transform range [46]. Thus, the Fourier transform can give only a rough idea about the distribution of neighboring atoms around the absorbing center and its complete interpretation is possible only through simulation [46, 48–51].

Currently, a number of approaches are used to determine the structural parameters from the EXAFS component of $\chi(k)$ selected with the use of Fourier filtration. The validity of these approaches depends on the admissibility of approximations used in simulation. The methods that are considered below are implemented in the EDA software package [32–34] and intended to analyze EXAFS signals of the first coordination sphere. Their applicability to the analysis of far coordination spheres is limited by multiple scattering effects, which are determined by the contributions of polyatomic distribution functions.

It is well known that multiple scattering effects are always present after the first structural peak in a Fourier transform [46–48]. In strongly disordered systems, the main contribution is from the multiple scattering effects in the first coordination sphere, whereas, in ordered systems, multiple scattering effects in the second and subsequent spheres can be additionally observed. A striking example of systems in which multiple scattering effects manifest themselves are compounds with perovskite structure (ReO_3, Na_xWO_3, FeF_3) and aqueous solutions of some transition elements [46, 48, 51–55]. A specific feature of these systems is the presence of linear or close to linear atomic chains, whose presence leads to enhancement of multiple scattering as a result of the so-called focusing effect. This effect, whose nature lies in the anisotropy of the atomic scattering amplitude, manifests itself in a significant increase in the photoelectron wave amplitude (and, correspondingly, the amplitude of EXAFS oscillations) in the case of forward scattering [46, 52].

Ab initio calculations of L_I- and L_{III}-edge EXAFS signals of Re in ReO_3 by the multiple scattering method [46, 48] showed that the contributions of multiple scattering in O–Re_0–O and Re_0–O–Re linear chains (the zero subscript indicates the absorbing atom) are very significant and determine to a large extent the intensity of peaks in a Fourier transform located, respectively, at 2.5 and 3.5 Å (Fig. 14). Furthermore, it has been found that the large amplitude of an EXAFS signal beyond the L_{II} edge and its proximity to the L_I edge ($E(L_I$–Re) – $E(L_{II}$–Re) = 568 eV) lead to an overlap of the L_I and L_{II} EXAFS oscillations in the region beyond the L_I edge. A similar situation was observed in some tungsten oxides [52, 54]. An analysis of the K-edge EXAFS spectrum of Fe in FeF_3, which has a rhombohedrally distorted

ReO_3-like structure, made it possible to find (owing to the multiple scattering effects) the contribution of Fe atoms located at a very far distance (7.5 Å) from the absorbing atom [53, 54]. In this case, multiple scattering occurs in the Fe_0–F–Fe–F–Fe atomic chains, and this effect is referred to as superfocusing [52].

In disordered systems (glasses [56], amorphous films [57–59], solutions [51]), multiple scattering effects are dominant in the first coordination sphere. In the case of octahedral coordination of an absorbing atom, as in the previous case, the main contribution is from the signals of multiple scattering in the O–W_0–O [27, 28], O–Mo_0–O [27, 28], O–Ir_0–O [27, 28], and O–Zn_0–O [51] atomic chains, which are close to linear. The contribution of multiple scattering effects from far coordination spheres is quenched owing to the structural and dynamic disorder. An example of calculation of multiple scattering effects for an octahedral cluster ZnO_6 is shown in Fig. 15. It can be seen that, along with the single-scattering signal *SS*1, there is a significant contribution from double-scattering (*DS*1 and *DS*2) and triple-scattering (*TS*1 and *TS*4) signals, which are responsible for the appearance of peaks in the Fourier transform of the *K*-edge EXAFS signal of zinc in an aqueous solution [51]. Thus, the possible presence of multiple scattering contributions in the region of far coordination spheres complicates the analysis of their EXAFS signals significantly. Therefore, in this case, correct application of the techniques described below requires careful estimation of possible errors related to the neglect of multiple scattering effects.

The EXAFS signal from the first coordination sphere of an absorbing atom can be interpreted in most cases within the formalism of single scattering of spherical waves [29–31]. Despite the simplicity of this model, there are no unambiguous procedures for analysis that would make it possible to obtain reliable structural information about the radial distribution function for the first coordination sphere in an arbitrary compound.

Currently, several approaches to analysis of EXAFS signals are widely used in practice: (i) a group of model-dependent methods based on parametrization of a radial distribution function in the form of an analytic function (for example, a Gaussian) [59, 60] or a cumulant expansion [61–64]; (ii) a group of model-independent methods that allow ab initio reconstruction of a radial distribution function, for example, the regularization method [65–67], freestyle Monte Carlo method [68] (that is reverse to the Monte Carlo method [69]), and the constrained nonlinear optimization method [32–34]; and (iii) the splice method [70, 71].

The splice method is singled out because it is based on the model-independent procedure of inversion of an EXAFS signal but uses a limited cumulant expansion for reconstruction of the EXAFS signal in the range from zero to the smallest experimentally accessible value of the wave vector. These three groups of methods (Fig. 11) are implemented in the EDA software package [32–34].

The first group is covered by the EDAFIT program, which uses a fast algorithm of conditional nonlinear optimization by the least-squares method [34]. This program is based on the multicomponent Gaussian/cumulant model in the single-scattering approximation [29–31]:

$$\chi(k) = \sum_i (N_i S_0^2)/(kR_i^2) F_i(\pi, k, R_i)$$
$$\times \exp[-2\sigma_i^2 k^2 + (2/3)C_{4i}k^4 - (4/45)C_{6i}k^6]$$
$$\times \exp[-2R_i/\lambda(k)] \sin[2kR_i - (4/3)C_{3i}k^3$$
$$+ (4/15)C_{5i}k^5 + \Psi_i(\pi, k, R_i)],$$

where N_i is the number of atoms in the ith group, located at a distance of R_i from the absorbing atom with a mean-square deviation σ_i of the distance; C_{3i}, C_{4i}, C_{5i}, and C_{6i} are the distribution cumulants that make it possible to approximate the contribution of the effects of anharmonic vibrations and/or non-Gaussian disorder; $F_i(\pi, k, R_i)$ is the amplitude of backscattering from atoms of the ith group; $\Psi_i(\pi, k, R_i) = \psi_i(\pi, k, R_i) + 2\delta_l(k) - l\pi$ is the phase shift, which contains contributions from the absorbing ($2\delta_l(k)$ and scattering $\psi_i(\pi, k, R_i)$ atoms (the angular momentum l of a photoelectron is 1 in the case of K and L_I edges and 2 or 0 in the case of $L_{\mathrm{II, III}}$ edges); $\lambda(k)$ is the photoelectron mean free path; and S_0^2 is the factor characterizing the change in the wave function of $(n-1)$ electrons upon excitation of the nth electron (generally, $S_0^2 = 0.6$–0.95). The structural model parameters N_i, R_i, σ_i, C_{3i}, C_{4i}, C_{5i}, and C_{6i} are variables. The amplitude $F_i(\pi, k, R_i)$ and the phase $\Psi_i(\pi, k, R_i)$ can be either taken from tables [72, 73], calculated theoretically via available programs (EXCURVE [36, 37], FEFF [38–41], GNXAS [42–45], MSCALC [74], MSXAS [75, 76]), or selected from the EXAFS spectrum of a reference compound [77]. The latter two approaches are preferential. The best results can be obtained by optimization of the theoretically calculated amplitude and phase with the use of a reference compound. As a result, exact and noiseless functions $F_i(\pi, k, R_i)$ and $\Psi_i(\pi, k, R_i)$ can be simultaneously obtained. Note that, if the amplitude and phase are calculated with the use of a complex exchange correlation potential (for example, of the Hedin–Lundqvist type [38, 74]), they automatically contain the contribution from the processes of inelastic scattering of a photoelectron and determining its mean free path $\lambda(k)$. In this case, the factor $\exp[-2R_i/\lambda(k)]$ should be excluded from the model. This model is valid for the compounds whose radial distribution functions can be expanded in several Gaussian or Gaussian-like peaks.

The splice method [70, 71] is based on the determination of the radial distribution function $G(R)$ by inversion of the reduced EXAFS function $\chi'(k)$ using the Fourier transformation:

$$G(R_i) = \int \chi'(k) \exp(-2ikR_i) dk,$$

where $\chi'(k) = \chi(k) k R_i^2 \exp[i\Psi(\pi, k, R_i)]/\{S_0^2 F(\pi, k, R_i)\exp[-2R_i/\lambda(k)]\}$ and integration is from zero to infinity. Since an experimental EXAFS signal is generally set in the interval from $k_{min} > 0$ to $k_{max} \sim 10$–20 Å^{-1} and its amplitude decreases with an increase in the wave vector **k**, integration assumes that $\chi(k > k_{max}) = 0$. The values $\chi(k < k_{min})$ are interpolated on the basis of the cumulant model, whose parameters are found from the criterion of best agreement with experiment in the interval from k_{min} to k_{max}. The accuracy in determining the radial distribution function is limited by two factors: (i) admissibility of the use of the cumulant approximation in the interval $0 < k < k_{min}$ and (ii) the value of an experimental EXAFS signal at $k = k_{max}$. Indeed, if $|\chi(k_{max})| \gg 0$, cut-off of the function $\chi(k)$ at $k = k_{max}$ leads to distortion of the desired radial distribution function in integration. This effect is shown by the example of the model radial distribution function composed of two Gaussian peaks with the parameters $N_1 = 2$, $R_1 = 1.8$ Å, $\sigma_1 = 0.05$ Å, $N_2 = 1$, $R_2 = 2.1$ Å, and $\sigma_2 = 0.06$ Å in Fig. 16. It can be seen well that, with a decrease in the upper integration limit k_{max} (in this case, this decrease is equivalent to an increase in the amplitude of the EXAFS signal at $k = k_{max}$), the discrepancy between the model and obtained radial distribution functions increases. The splice method is implemented in the EDA package (EDAFT and EDAPLOT programs).

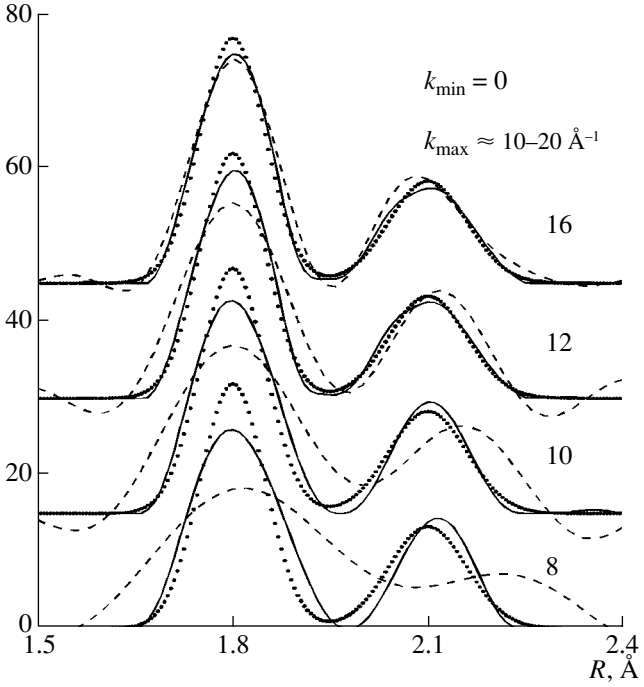

Fig. 16. Effect of the upper limit k_{max} of the EXAFS signal range on the shape of the radial distribution function obtained by the splice (dashed lines) and model-independent (solid lines) methods. The model radial distribution function is shown by circles.

The model-independent methods allowing ab initio reconstruction of the radial distribution function are represented in the EDA package by the program of constrained nonlinear optimization (EDARDF) [32–34]. In the case of an arbitrary radial distribution function, the EXAFS signal is described by the expression [78, 79]

$$\chi(k) = S_0^2 \int [G(R)/(kR^2)] F(\pi, k, R) \times \sin[2kR + \Psi(\pi, k, R)] dR,$$

where the radial distribution function $G(R) = 4\pi R^2 \rho_0 g(R)$ corresponds to the number of atoms located in a spherical layer from R to $R + dR$ around the absorbing atom. An arbitrary initial radial distribution function $G(R)$ is set in the interval from R_{min} to R_{max} with a step $\Delta R \le 1/(2k_{max})$ and the desired radial distribution function is determined with an iterative procedure minimizing the value $S = \sum_k [\chi_{sim}(k) - \chi_{exper}(k)]^2$ with additional limitations: $G(R) \ge 0$ and $G(R)$ should be a smooth function. When necessary, one can introduce an additional condition for the area $G(R)$ (i.e., on the total coordination number). In most practical cases, the radial distribution function of the first coordination sphere decreases to zero at the ends of the interval $[R_{min}; R_{max}]$. Hence, correct integration can be performed. Note that this method has no limitations on the shape of the radial distribution function.

Below, we will give some examples of using the above-considered methods to reconstruct the radial distribution function in model and actual systems.

Figure 16 shows the results of application of the model-independent method in comparison with the splice method. It can be clearly seen that the boundedness of an EXAFS signal affects the former method much weaker. In fact, this parameter leads to broadening of radial distribution function peaks, an effect that is naturally related to a decrease that occurs in the resolution in the R space owing to the shortening of the EXAFS signal.

The Gaussian and cumulant models are compared with the model-independent method in Fig. 17. The model radial distribution functions were chosen so as to reproduce the following shapes of $G(R)$ (which are often met in actual compounds): (i) a single Gaussian peak ($N = 1$, $R = 1.8$ Å, $\sigma = 0.06$ Å) (Fig. 17a), (ii) two unresolved Gaussian lines ($N_1 = 2$, $R_1 = 1.8$ Å, $N_2 = 1$, $R_2 = 1.9$ Å, $\sigma_1 = \sigma_2 = 0.06$ Å) (Fig. 17b), (iii) two Gaussian peaks ($N_1 = 2$, $R_1 = 1.8$ Å, $\sigma_1 = 0.05$ Å; $N_2 = 1$, $R_2 =$

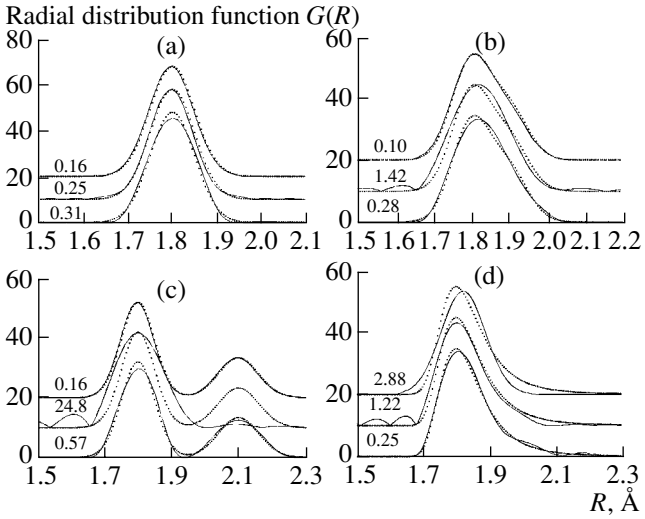

Fig. 17. Comparison of different methods for determining the radial distribution function from an EXAFS signal for radial distribution functions of different shapes: the model radial distribution function (circles), the Gaussian model (upper solid lines), the cumulant model (middle solid lines), and the model-independent method (lower solid lines). Numbers show the degree of agreement between the obtained and model radial distribution functions,

$$\varepsilon = 100\% \quad \frac{\Sigma(\mathrm{RDF}_{\mathrm{calc}} - \mathrm{RDF}_{\mathrm{mod}})^2}{\Sigma(\mathrm{RDF}_{\mathrm{mod}})^2} .$$

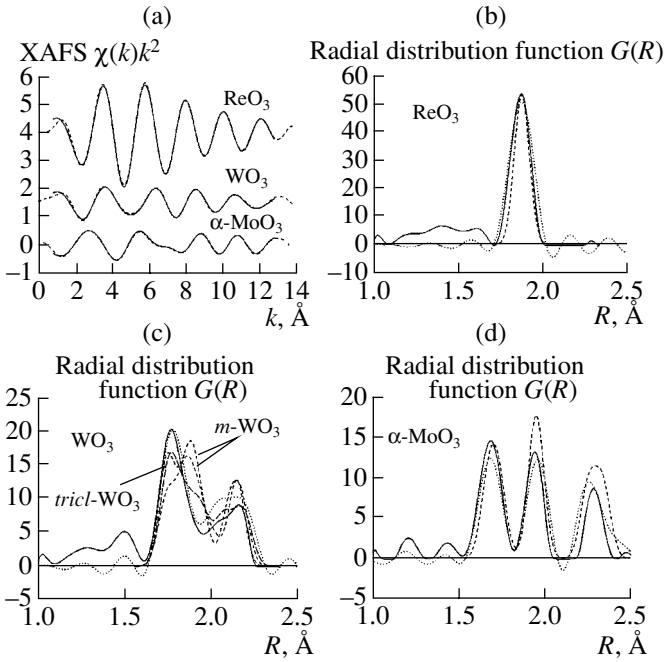

Fig. 18. EXAFS signals $\chi(k)k^2$ of the first coordination sphere of rhenium in ReO_3 (Re L_3 edge), tungsten in WO_3 (W L_3 edge), and molybdenum in MoO_3 (Mo K edge) obtained by (solid lines) the model-independent method in comparison with (dashed lines) experiment and the radial distribution functions $G(R)$ of the first coordination sphere obtained by the (circles) splice and the (solid lines) model-independent methods in comparison with the radial distribution functions derived from (dashed lines) the X-ray and neutron diffraction data.

2.1 Å, $\sigma_2 = 0.06$ Å) (Fig. 17c), and (iv) an asymmetric radial distribution function that is similar to those observed in superionic materials (Fig. 17d). It can be seen that, in the cases where the distribution shape differs from the analytic model, discrepancies in the position, intensity, and width of radial distribution function peaks are observed: the Gaussian model cannot describe an asymmetric radial distribution function, whereas the cumulant model poorly describes two-Gaussian distributions. Only the model-independent method reproduces all types of radial distribution functions equally well.

Figure 18 shows the application of the splice method and the model-independent approach to three actual crystalline compounds: rhenium, tungsten, and molybdenum trioxides. The structural peaks of the radial distribution functions reconstructed by both methods are in satisfactory agreement with each other and with the peaks of the radial distribution functions constructed according to the X-ray and neutron diffraction data. Moreover, the radial distribution function obtained in the case of tungsten trioxide makes it possible to distinguish triclinic and monoclinic modifications of WO_3 unambiguously, which may coexist at room temperature (at which the experiment was carried out). Note also that there is very good agreement between the EXAFS signals from the first coordination sphere obtained from experimental data and calculated by the model-independent method. The nonstructural peaks in the radial distribution functions in the range of small distances (Fig. 18) reflect errors in the experimental EXAFS signals. Note that the radial distribution functions obtained by the splice method have regions with negative values, which arise in the Fourier transformation owing to the very short range of the experimental spectrum.

In simulation of EXAFS signals, the problem of ambiguous interpretation often arises, which is related to the fact that some models give good agreement with experimental results. In addition, when the multicomponent Gaussian or cumulant model is used, the problem of choosing the minimum number of components allowing for adequate description of an experimental signal exists. To solve these problems, it is convenient to use the Nyquist and Fisher criteria [34, 80]. The Nyquist theorem limits the maximum number of model parameters that can be used to analyze an experimental signal set in the intervals Δk and ΔR: $M_{\max} = (2\Delta k \Delta R)/\pi + 2$. For example, in the case of an EXAFS signal from the first coordination sphere in rhenium trioxide, $\Delta k = 13 - 1 = 12$ Å^{-1} (Fig. 18) and $\Delta R = 1.9 - 0.7 = 1.2$ Å (the interval of the first peak in Fig. 14); hence, $M_{\max} \sim 11$. This number far exceeds the true number of parameters (three in the case under consideration: N, R, and σ) that

are necessary to describe the first coordination sphere of rhenium, which is composed of six equidistant oxygen atoms. Application of the Fisher criterion in framework of dispersion analysis makes it possible to find a model with a minimum number of parameters adequately describing experimental data. Let the number of parameters of the two models $\chi_1(k)$ and $\chi_2(k)$ be M_1 and M_2, respectively ($M_2 > M_1$). Then, the dispersions D_1 and D_2 are

$$D_j = [M_{\max}/(n(M_{\max} - M_j))]\sum_i [\chi(k_i) - \chi_j(k_i)]^2,$$
$$j = 1, 2, \quad i = 1, \ldots, n.$$

According to the $F_{0.95\%}$-Fisher criterion, the model $\chi_2(k)$ is accepted when $D_1/D_2 > F_{0.95\%}$. The values of $F_{0.95\%}$ are tabulated [80]. In the EDA package, the procedure of dispersion analysis is implemented in the FTEST program.

Many experimental studies give the following estimates of averaged errors for the main structural parameters in the first coordination sphere: $\Delta R \sim 0.01$ Å for interatomic distances R_j; $\frac{\Delta N}{N} \geq 10\%$ for the number of atoms N, and $\frac{\Delta\sigma}{\sigma} \geq 20\%$ for the Debye–Waller factor.

For subsequent spheres, the errors sharply increase and are determined in many respects by the type of the structure and approximations used. In most cases, the EXAFS function gives the most exact description of the microscopic structure of the condensed state near absorbing atoms at distances up to 4–6 Å and no larger than 10–15 Å.

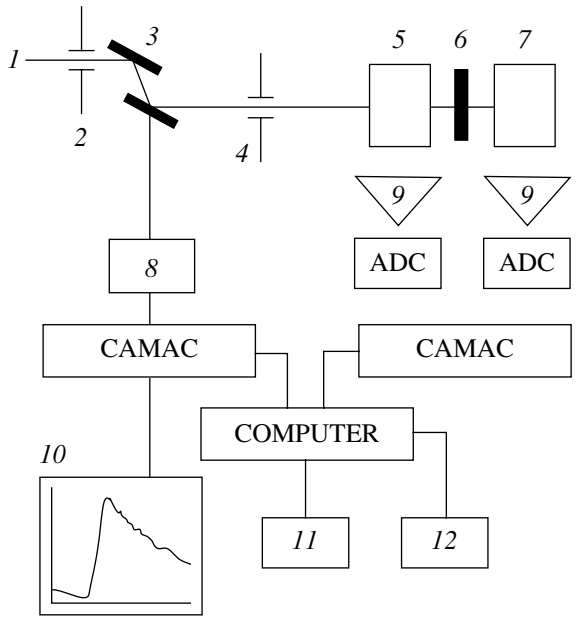

Fig. 19. Block diagram of the EXAFS spectroscopy station: (*1*) synchrotron radiation, (*2*, *4*) collimators, (*3*) monochromator, (*5*) monitor, (*6*) sample, (*7*) detector, (*8*) stepper motor, (*9*) amplifier, (*10*) display, (*11*) terminal, and (*12*) plotter printer.

3. BASIC SCHEMES OF EXAFS SPECTROMETERS USING SYNCHROTRON RADIATION BEAMS

Let us consider the following experimental schemes for measuring EXAFS functions based on detection of different channels of excitation of a solid by incident X-rays:

(i) Measurement of the transmission function, when the total transmittance $T(E_\gamma)$ of the object under study with a thickness L_x for radiation of specified energy $E_\gamma = \hbar\omega$ is recorded. The dependence $T(E_\gamma)$ is used to reconstruct the dependence of the absorption coefficient μ on the X-ray photon energy. $L_x\mu = \ln\left(\frac{I_0(E_\gamma)}{I(E_\gamma)}\right)^{1/x}$, where $I_0(E_\gamma)$ and $I(E_\gamma)$ are the radiation intensities without and with a sample, respectively. Figure 19 shows the scheme for measuring EXAFS spectra in transmission [27].

(ii) Determination of the EXAFS function from measurement of the decay of the excited state (formed as a result the absorption of an X-ray photon) through different channels (fluorescence, secondary-electron emission, optical luminescence).

In measurements of the EXAFS function in transmission, the error in determining the absorption coefficient μ_x is estimated from the expression $(\Delta\mu_x)^2 = \frac{3.223}{(I_0)}(\mu_x + \mu_m)^2$ [24], where μ_x is the absorption coefficient of the object under study, I_0 is the intensity of incident radiation, and μ_m is the absorption coefficient of the matrix in which the sample is located. $\mu_m = N_m\sigma_m$ and $\mu_x = N_x\sigma_x$, where N_m and N_x are the numbers of matrix and object atoms, respectively, and σ_m and σ_x are the X-ray absorption cross sections of the matrix and object, respectively.

The formula for $\Delta\mu_x$ was derived under the condition that the sample thickness L_x ensures the minimum error $\frac{\Delta\mu_x}{\mu_x}$ ($L_x = \frac{2.557}{\mu_x}$). For the second measurement scheme, where the secondary particle yield upon X-ray absorption is determined, we have [24]

$$(\Delta\mu_x)^2 = \frac{1}{(I_0)}\left(\frac{2\mu_x}{FL_x}\right),$$

where F is the total efficiency of detection of secondary particles ($F \leq 1$).

In transmission measurements of biological samples composed of an absorbent with the absorption coefficient μ_m and the object of study with $\mu_x \ll \mu_m$, the signal-to-noise ratio is $(S/N) = (I_0 t)^{1/2} 2e^{-1} \frac{\mu_x}{\mu_m}$ (at the optimal relation for the sample thickness $\mu_m L_x = 2$).

For example, at the incident radiation intensity $I_0 \sim 10^{11}$ photons/s, $t = 1$ s, and $S/N = 3$, the above equation gives the value $\frac{\mu_x(\omega)}{\mu_m} = 1.3 \times 10^{-5}$. Hence, this mode can be used to measure the content of atoms studied at a level of 10^{-3}% of the main content.

In measurements in the fluorescent mode using a narrow-band detector, at the energy ω_F of the fluorescence signal, the signal-to-noise ratio is [24]

$$S/N = \frac{I_0 f F \mu_x(\omega) \Omega}{(\mu_m(\omega) + \mu_m(\omega_F))4\pi},$$

where f is the fluorescence yield, F is the detector sensitivity, and Ω is the solid angle of measurement of the secondary radiation.

Estimation for the fluorescent mode at $I_0 = 10^{11}$ photons/s, $t = 1$ s, $F\Omega/4\pi = 0.01$, and $f = 0.1$ gives the ratio $\frac{\mu_x}{\mu_m} = 4 \times 10^{-8}$. This value is three orders of magnitude larger than that obtained by transmission measurement. Analysis of the formulas for necessary statistical accuracy shows that the radiation source intensity is the decisive factor for the time required to collect the necessary statistics. For laboratory EXAFS spectrometers, which use radiation sources in the form of X-ray tubes with an intensity of about 10^5 photons/s in a line with the resolution $\delta E = 5$–6 eV, the EXAFS-spectrum collection time is 10–12 h.

Significant progress in EXAFS spectroscopy has been achieved with synchrotron radiation whose luminous characteristics significantly exceed continuous sources based on X-ray tubes. Figure 20 shows the luminous characteristics of two synchrotron radiation sources: DCI (France) ($E_e = 1.8$ GeV, $I_e = 200$ mA) and Sibir'-2 (Russia) ($E_e = 2.5$ GeV, $I_e = 200$ mA). Radiation with such brightness makes it possible to measure EXAFS spectra with a collection time from 10 to 10^{-3} s, depending on the spectrometer scheme.

To measure the EXAFS function $\chi(E_\gamma)$ in both transmission and fluorescence modes, it is necessary to monochromize the incident radiation E_γ with the energy resolution ΔE_0, which is determined by the size R_j of the first coordination sphere of the object under study. The necessary resolution for most objects should be $5 \text{ eV} \le \Delta E_0 \le 12$ eV.

The continuous spectrum of synchrotron radiation was monochromized with the use of Bragg reflection of X-rays from crystals with different values of interplanar spacing $2d_{hkl}$. The wavelength and the reflection angle are related by the expression $2d \sin\theta = n\lambda_x$, where n is the reflection order. The degree of monochromatization ΔE is determined by the width of the cone of reflected and incident radiation [27]:

$\frac{\Delta E}{E} = \cot\theta \Delta\theta$, where $\Delta\theta$ is the angular dispersion of the radiation reflected from the crystal.

For a monochromator, $\Delta\theta$ is determined by three terms: the angular spread $\Delta\theta_s$ of the incident radiation with respect to the Bragg angle (θ_s is controlled by the channel acceptance and the radiation source size), the angular spread $\Delta\theta_m$ controlled by the input monochromator aperture; and the angular width Ω_x of the reflected radiation (Darwin width), which is given by the expression $\Omega_x(\lambda_x) = \frac{2}{\sin\theta} \frac{r_0 \lambda_x^2}{\pi v} F_c$, where F_c is the structural factor of a crystal, v is the unit-cell volume, and r_0 is the classical electron radius.

The Darwin curve determines the resolution limit of a monochromator: $\frac{\Delta E}{E} = \Omega_x \cot\theta$.

The scheme of a double-crystal monochromator is widely used in EXAFS spectroscopy. In this scheme, the first crystal acts as a direct monochromator, while the second one is used to filter the highest harmonics at small angular rotations with respect to the first crystal within the Darwin width of the reflection curve.

As mentioned above, in absorption spectroscopy, the resolution of a monochromator for the XANES and EXAFS regions is determined by different physical processes. For the XANES region, the resolution width should not exceed the intrinsic linewidth, which is

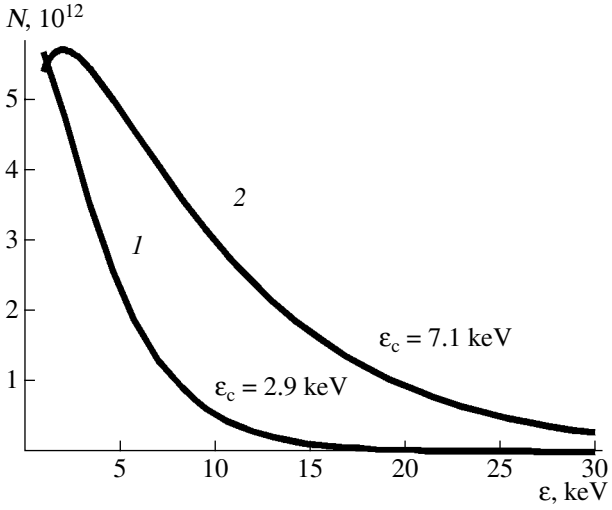

Fig. 20. Luminous characteristics of the synchrotron radiation spectra of the (*1*) DSI ($E_e = 1.8$ GeV) and (*2*) Sibir'-2 ($E_e = 2.5$ GeV) sources.

determined by the lifetime of the core hole level. $\Delta E_\tau = 2 \times 10^{-4} E_{BE}$, where E_{BE} is the binding energy of the B level (for the energy range 7–10 keV, ΔE = 1.4–2 eV). For the EXAFS region, the monochromator resolution ΔE_0 should exceed the fine-structure energy scale $\Delta E_{EXAFS} = \frac{\hbar^2 \Delta k}{m} = \frac{\hbar^2 \pi k_{min}}{2mR_j}$, where k_{min} is the wave vector of an electron with the minimum energy 2 Å^{-1} and R_j is the radius of the first coordination sphere at 2 Å $\le R_j \le$ 5 Å and 5 eV $\le \Delta E_{EXAFS} \le$ 12 eV.

Figure 19 shows a schematic of the experimental EXAFS spectroscopy station on the synchrotron radiation beam with the energy E_e = 1.8 GeV in the DCI storage ring [46], which was used to investigate the structure of oxide compounds. This system uses a double-crystal monochromator of the parallel type. The resolution in the range 5–15 keV is $\Delta E/E \sim 10^{-4}$. In transmission, the EXAFS function is found with two proportional chambers measuring the radiation flux before and after the image (I_0 and I_x, respectively). The absorption coefficient is determined by the formula

$$L_x \mu_x(E) = \ln(I_0/I_x).$$

The time of measurement of the entire EXAFS spectrum depends of the sample type and is approximately 10 min. Measurement is performed step by step by a successive scan in energy.

An original scheme of an EXAFS spectrometer without mechanical wavelength tuning (energy-dispersive EXAFS) was reported in [81]. This scheme is based on the use of a bent monochromator crystal focusing X rays on a sample in some energy range ΔE. In this case, the spectrum of transmitted radiation is spatially expanded in the vicinity of the energy focus point. This spectral expansion is measured by a high spatial resolution detector.

The energy-dispersive EXAFS spectrometer has some advantages over the classical one:

(i) Mechanical scanning is absent: measurement of the energy dependence of the absorption spectrum is reduced to measurement of the spatial distribution of X rays transmitted through a sample.

(ii) At the minimum measurement time $t \sim 3$ ms, which is provided by modern solid-state position-sensitive detectors, this scheme makes it possible to analyze in situ effects of various external fields on the structure of solids.

(iii) There is a possibility of focusing radiation on a sample down to several micrometers in size. This possibility makes it possible, for example, to install a sample in a high-pressure chamber and investigate the effect of pressure on the short-range order.

Currently, in many synchrotron radiation centers, energy-dispersive EXAFS spectrometers have been developed [82, 83], which are used in a wide range of investigations on the physics and chemistry of catalysts, electrochemical processes, cryogenic crystals, magnetic structures, and phase transitions [84–86].

4. ENERGY-DISPERSIVE EXAFS SPECTROMETER

A specialized synchrotron radiation source at the Russian Research Centre Kurchatov Institute has been put into operation. This source has the following parameters of bending-magnet synchrotron radiation: the critical photon energy E_c = 7.1 keV and the maximum brightness $B = 2 \times 10^{14}$ photons/(s mm^2 mrad^2) in the band $\Delta\lambda/\lambda = 10^{-3}$ at the current of stored electrons I_e = 200 mA (the luminous characteristic is shown in Fig. 20).

An EXAFS-spectroscopy station based on the energy-dispersive scheme was designed in one of the source channels [83]. Figure 21 shows the optical scheme of the energy-dispersive spectrometer, whose main elements are a monochromator based on a bent crystal of length l with a varied radius of curvature R, an optical bench with a rotation axis aligned with the monochromator axis, and a 1D or 2D (depending on the problem under study) position-sensitive detector.

An important parameter of the energy-dispersive scheme of the EXAFS spectrometer is its energy measurement range ΔE. It is determined by the expression $\Delta E = (l/R - l\sin\theta/p)\cot\theta$, where l is the length of the monochromator crystal region exposed to X rays. The Bragg angle changes along the bent crystal and the radiation in this energy range is focused to the polychromatic point. Depending on the radius of curvature, ΔE ranges from 200 to 800 eV.

The main parameters of the EXAFS spectrometer are listed in Table 1.

The width of the energy focusing range is determined as $\Delta L = \Delta\theta(d + q)_{min} \simeq R\sin\theta(l/R - l\sin\theta/p)$, $\Delta L = l\sin\theta$ = 4 cm for ΔE = 700 eV.

In EXAFS spectroscopy of the radiation transmitted through a sample, measurement of the spectrum is reduced to measurement of the spatial distribution of X-ray intensity at the focus point, i.e., at the distance $(d + q)_{min}$ from the monochromator. If a photodiode array with 1024 elements and a length of measurement region of 20 mm is used, the energy per measuring unit is 0.4 eV/pixel.

After the polychromatic focus, X rays diverge in the horizontal plane along the rays of a circle centered at the point O of the polychromatic focus. If a slit that can be rotated with respect to the point O is installed on an optical bench with a rotation axis passing through the point O, this slit will pass, for each angle φ, radiation with a certain energy E_φ and the spectral width $\delta E = \partial E/\partial\varphi\delta\varphi$, where $\delta\varphi$ is the angular slit width.

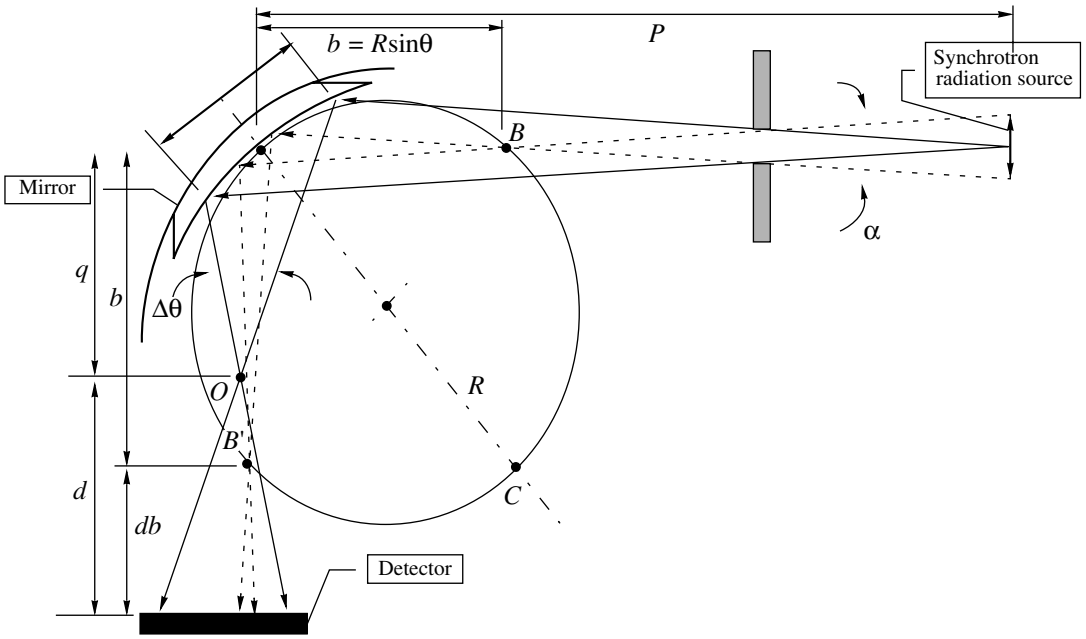

Fig. 21. Optical scheme of the energy-dispersive EXAFS spectrometer.

The energy-dispersive optical scheme makes it possible to implement two types of an EXAFS spectrometer [83].

Type I (Fig. 22) is a time-resolved EXAFS spectrometer in transmission; here, a sample is installed at the polychromatic focus *O* on a rotating optical bench. The sample unit may include a pumped optical cryostat (4.7–300 K), a high-pressure chamber with diamond anvils, a magnetic chamber for measuring magnetic dichroism, a chamber for studying the processes of formation and growth of solid phase particles in aqueous and nonaqueous media, and a thermal-stimulation chamber for studying structural and chemical transformations of solid materials in the range 20–600°C in isothermal and nonisothermal modes. To separate the highest order X rays reflected from the monochromator, a reflecting mirror with a gold coating is used.

Type II (Fig. 22) is an EXAFS spectrometer with energy varied by scanning in angle φ with rotation of the second optical bench along a circle arc corresponding to a certain energy range ΔE.

Figure 23 shows the scheme implementing measurements of surface EXAFS spectra in the fluorescent mode. Here, a channel for measuring light excited by X rays is added, which makes it possible to study structural transformations of amorphous and poorly crystallized films of semiconductors, ferromagnets, ferroelectrics, etc.

Experiments performed at LURE with an energy-dispersive spectrometer [82] showed the possibility of simultaneous measurement of angular and energy spectra. Figure 24 presents the schemes of angular and energy measurements. The investigations performed showed that the resolution in the wave vector $q = 2\pi\sin\theta/\lambda$ is $\delta q \simeq 1.5 \times 10^{-3}$ Å^{-1}.

Thus, the energy-dispersive scheme makes it possible to carry out a wide complex of measurements, specifically, to record time-resolved EXAFS spectra (in order to observe the influence of various external effects on an object) with a energy resolution of 2–4 eV in the energy range 5–25 keV, EXAFS and scattering spectra with a resolution in the wave vector q of $\simeq 10^{-1}$–10^{-3} Å^{-1}, and EXAFS spectra of surface layers in the fluorescent and optical modes.

Figure 25 shows a photograph of the energy-dispersive EXAFS spectroscopy station.

To measure EXAFS spectra in transmission and surface reflection modes, a position-sensitive X-ray detector with cryogenic cooling has been developed on the basis of a multielement photodiode array [87]. Figure 26 shows the K_α and K_β synchrotron radiation spectra measured with this position-sensitive detector installed in the focal plane of the monochromator with a bent LiF crystal. An X-ray tube with a copper anode was used as a radiation source.

Table 1. Main parameters of the EXAFS spectrometer

Crystal type	Energy range, keV	Resolution, $\delta E/E$
Si(111)	5–15	$\simeq 10^{-4}$
Si(311)	7–30	$\simeq 10^{-4}$
Asymmetric Si(311), $a = -12$	7–30	$< 10^{-4}$

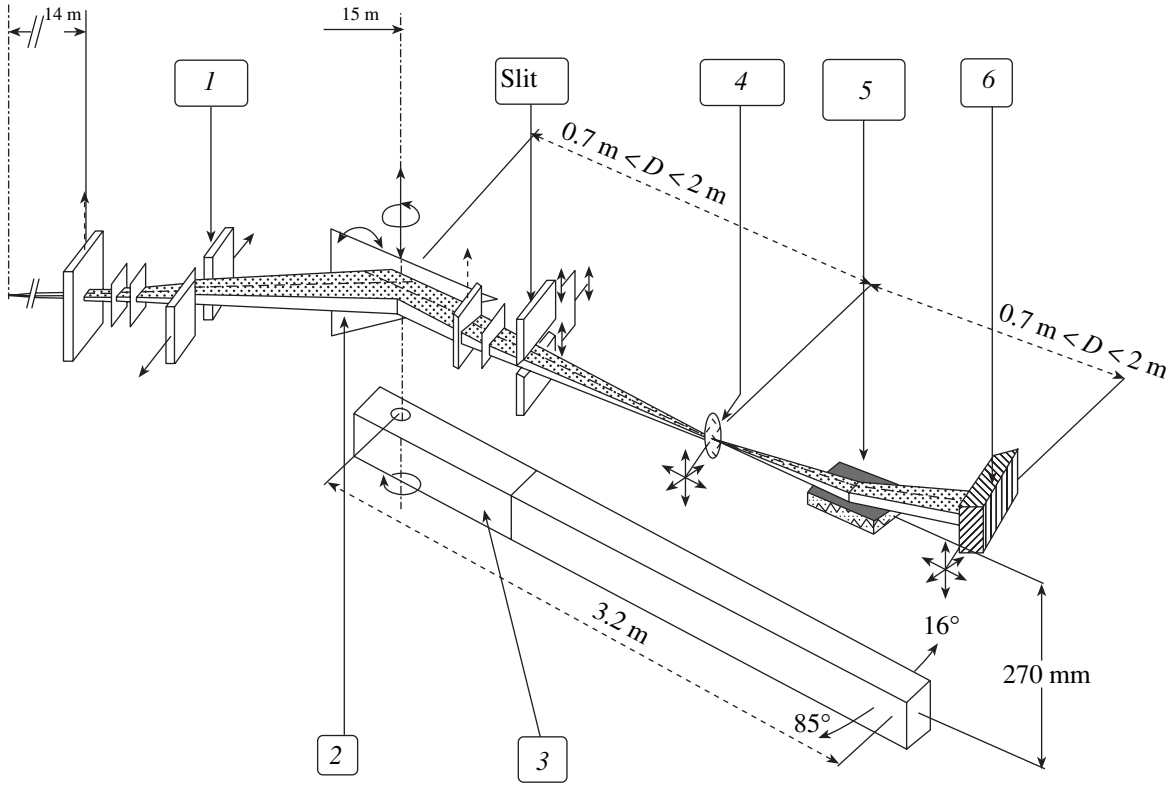

Fig. 22. Energy-dispersive EXAFS spectrometer: (*1*) input forming optics, (*2*) monochromator with a triangular Si crystal equipped with a bending attachment, (*3*) optical bench on aerostatic supports, (*4*) cryostat and a high-pressure chamber, (*5*) block of mirrors, and (*6*) cryogenic 2D position-sensitive detector.

5. LOCAL STRUCTURE OF TUNGSTEN AND MOLYBDENUM OXIDES

In this section, we will consider the application of EXAFS spectroscopy to the study of the local structure of oxides (crystals, glasses) and thin amorphous films of tungsten and molybdenum. This class of materials is of great fundamental and practical interest.

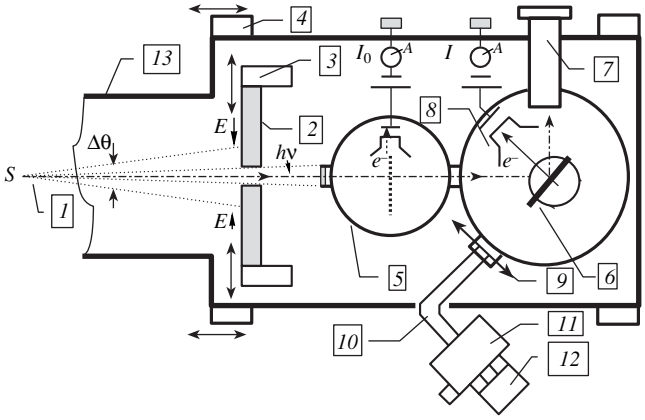

Fig. 23. Energy-dispersive EXAFS spectrometer operating in the fluorescent mode for studying surface layers: (*1*) radiation source, (*2*) gap, (*3*) opening mechanism, (*4*) table rotation mechanism, (*5*) monitor chamber, (*6*) sample, (*7*) Ge(Li) detector, (*8*) electron counter, (*9*) lens, (*10*) optical fiber, (*11*) monochromator, (*12*) photoelectron multiplier and (*13*) body.

Tungsten and molybdenum are transition elements, whose physical properties are determined by the number of external *d* electrons and the degree of their localization. Characteristic features of tungsten and molybdenum oxides are the possibility of changing the valence of metal ions by an external action, which is accompanied by a change in the optical and electrical properties, and the existence of compounds with a mixed valence. In addition, in disordered structures (glasses and amorphous films), these oxides can play the role of both a modifier and a network former. It is important that, in contrast to such classical network-forming oxides as SiO_2, P_2O_5, and B_2O_3 with a structure formed on the basis of polyhedra with an oxygen coordination of no more than four atoms, the coordination of tungsten and molybdenum ions playing the role of network formers often reaches octahedral. Owing to the above-mentioned properties, tungsten and molybdenum oxides are used in electrochromic systems, catalysts, and sensors [88]. Therefore, it is very important to understand the relationship between the physical properties and structure of these compounds. The use of EXAFS spectroscopy for this purpose is justified by the fact that most practically important properties of tung-

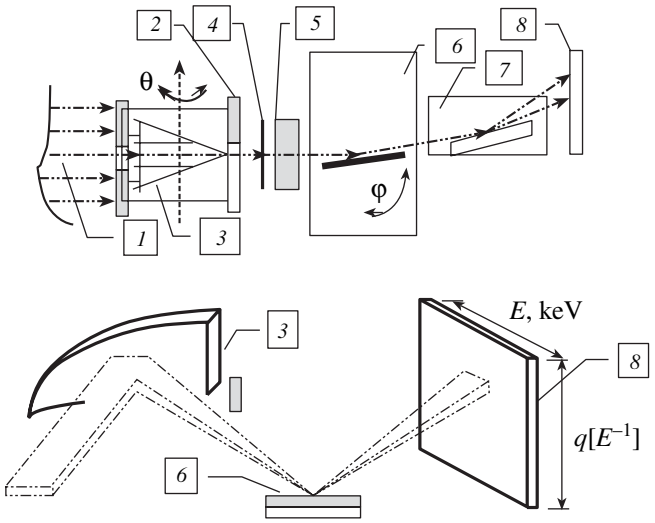

Fig. 24. Scheme for measuring the angular and energy characteristics of scattered X-rays in the energy-dispersive mode: (*1*) input synchrotron radiation beam, (*2*) exit slit, (*3*) monochromator crystal, (*4*) beryllium window, (*5*) gate, (*6*) sample unit, (*7*) mirror unit, and (*8*) 2D position-sensitive detector.

Fig. 25. Energy-dispersive EXAFS station: an X-ray monochromator, input X-ray optics, a mirror, and a detector are mounted on a granite mobile optical bench.

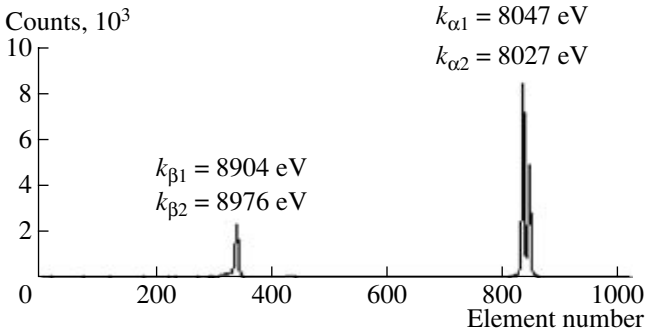

Fig. 26. Emission spectrum of a compact X-ray tube with a copper anode operating at a voltage of 30 kV and a current of 25 μA. The dispersive element is $SiO_2(1340)$; R = 100 mm.

sten and molybdenum oxides are determined by changes in the local atomic and electronic structures of metal ions.

In most compounds considered below, the metal ion is in the maximum oxidation state and has the electronic configuration d^0. The basis structural element of all these compounds except $CaWO_4$ is the metal–oxygen octahedron [MeO_6] (Me = W, Mo). It is well known [89] that octahedrally coordinated d^0 ions of transition metals are generally shifted from the center of the octahedron, i.e., occupy off-center positions. A comparison of the local environment of different d^0 ions (Ti^{4+}, Zr^{4+}, V^{5+}, Nb^{5+}, Ta^{5+}, Mo^{6+}, and W^{6+}) suggests that a distortion of the coordination octahedron MeO_6 increases with an increase in the formal ion charge and a decrease in the ionic radius [94]. Previously, four causes of distortion have been considered [94].

The main contribution, which is explained by the second-order Jahn–Teller effect [90], is from the electronic structure of the transition-metal ion. In a solid, as a result of mixing of free *d* orbitals of the cation and occupied *p* orbitals of ligands, a set of different electronic configurations with closely spaced quasi-degenerate energy levels arises, whose order is determined by the cation environment. Therefore, a displacement of the cation from the octahedron center may remove degeneracy and decrease the total energy of the system. Along with the second-order electronic Jahn–Teller effect, the displacement of a metal ion from the center of the octahedron can be caused by three more structural factors [94]: the type and number of chemical bonds with the neighboring atoms; structural incommensurabilities, which manifest themselves in the form of lattice stresses (removal of these stresses leads to deformation of interatomic bonds); and direct cation–cation interaction (repulsion) in the case where two octahedra share an edge or a face.

In each specific case, the degree of distortion of the coordination octahedron [MeO_6] depends on both the magnitude of the electronic effect and the ability of the structure to accumulate distortions. The causes of the distortion that have an electronic and structural nature supplement each other and cannot always be separated easily. The electronic effect does not control the direction of metal ion displacement from the center of the octahedron. This displacement is determined by the causes of distortion that have a structural nature or, in their absence, corresponds to a particular direction and thus decreases the symmetry of the entire structure [94].

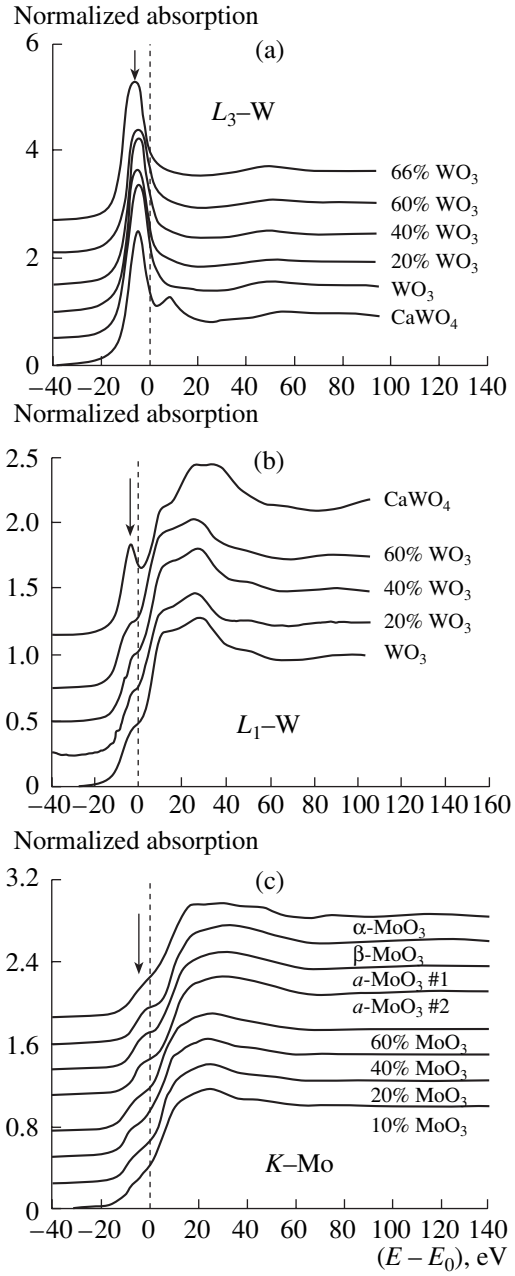

Fig. 27. XANES spectra of (a, b) the $L_{1,3}$ edges of tungsten and (c) the *K* edge of molybdenum in barium tungsten phosphate glasses and calcium molybdenum phosphate glasses, respectively. The vertical arrows indicate the positions of the white lines. The white line intensity at the L_1 and *K* edges increases with increasing distortion of [MeO_6] octahedra (*Me* = W, Mo).

With a decrease in the oxidation state of a metal ion to 5+, its *d* orbitals become filled to the electronic configuration d^1. As a result, the local structure significantly changes. If a *d* electron is localized, the degeneracy is removed as a result of the first-order Jahn–Teller effect [91] and the local symmetry increases (in comparison with the d^0 configuration) to tetragonal. In the case of a delocalized *d* electron, [MeO_6] octahedra are completely symmetrized and *d* electrons are involved in the metallic conduction. In both cases, the metal ion is located at the center of the octahedron.

Thus, it is of great interest to determine the sensitivity of EXAFS spectroscopy to different types of distortion of the coordination octahedron [MeO_6]. To this end, the local structure of tungsten and molybdenum ions in tungsten phosphate glasses (40 BaO–40 P_2O_5–20 WO_3 (20% WO_3), 30 BaO–30 P_2O_5–40 WO_3 (40% WO_3), 20 BaO–20 P_2O_5–60 WO_3 (60% WO_3), and 34 P_2O_5–66 WO_3 (66% WO_3)), molybdenum phosphate glasses (45 CaO–45 P_2O_5–10 MoO_3 (10% MoO_3), 40 CaO–40 P_2O_5–20 MoO_3 (20% MoO_3), 30 CaO–30 P_2O_5–40 MoO_3 (40% MoO_3), and 20 CaO–20 P_2O_5–60 MoO_3 (60% MoO_3)), polycrystalline compounds (monoclinic WO_3, cubic $Na_{0.6}WO_3$, $CaWO_4$, α-MoO_3, and β-MoO_3), and amorphous thin films of *a*-WO_3 and *a*-MoO_3 has been investigated [91, 92].

The spectra were measured at the $L_{1,3}$ absorption edges of tungsten and the *K* absorption edge of molybdenum with synchrotron radiation of the ADONE (Italy) and LURE DCI (France) storage rings [92, 93]. The measurements were performed by the standard technique in transmission. X rays were monochromized with a single-block Si(220) or double Si(311) monochromator crystal, and their intensity was measured in two ionization chambers filled with either krypton or argon. All measurements were carried out at room temperature.

Figure 27 shows the near-edge X-ray absorption spectra. Near the tungsten L_3 absorption edge, a strong peak (the so-called white line) can be clearly seen. This peak corresponds to the allowed dipole transition from the $2p_{3/2}$(W) level to the quasi-bound mixed state 5*d*(W) + 2*p*(O), which is formed as a result the hybridization of tungsten 5*d* orbitals and oxygen 2*p* orbitals. At the same time, the transition from the 2*s* level of tungsten to the L_1 edge is dipole-forbidden and its intensity depends strongly on the magnitude of *pd* mixing, i.e., the covalence of the tungsten–oxygen bond and the degree of distortion of the [WO_6] octahedron. An analogous transition (1*s*(Mo) $\longrightarrow$ 4*d*(Mo) + 2*p*(O)) is observed at the molybdenum *K* edge. Its intensity is determined by the same factors as for the tungsten L_1 absorption edge. Thus, on the basis of the intensity of the white line at the *K* and L_1 absorption edges, one can qualitatively estimate the degree of distortion of the first coordination sphere of tungsten (molybdenum). As can be seen in Fig. 27, comparison of the XANES signals of glasses and crystalline oxides with a known structure makes it possible to conclude that the octahedral coordination of tungsten (molybdenum) ions in glasses and amorphous films is distorted. This conclusion is in good agreement with the fact that these ions have the d^0 (W^{6+}, Mo^{6+}) electronic configuration and with the structural EXAFS data (see below).

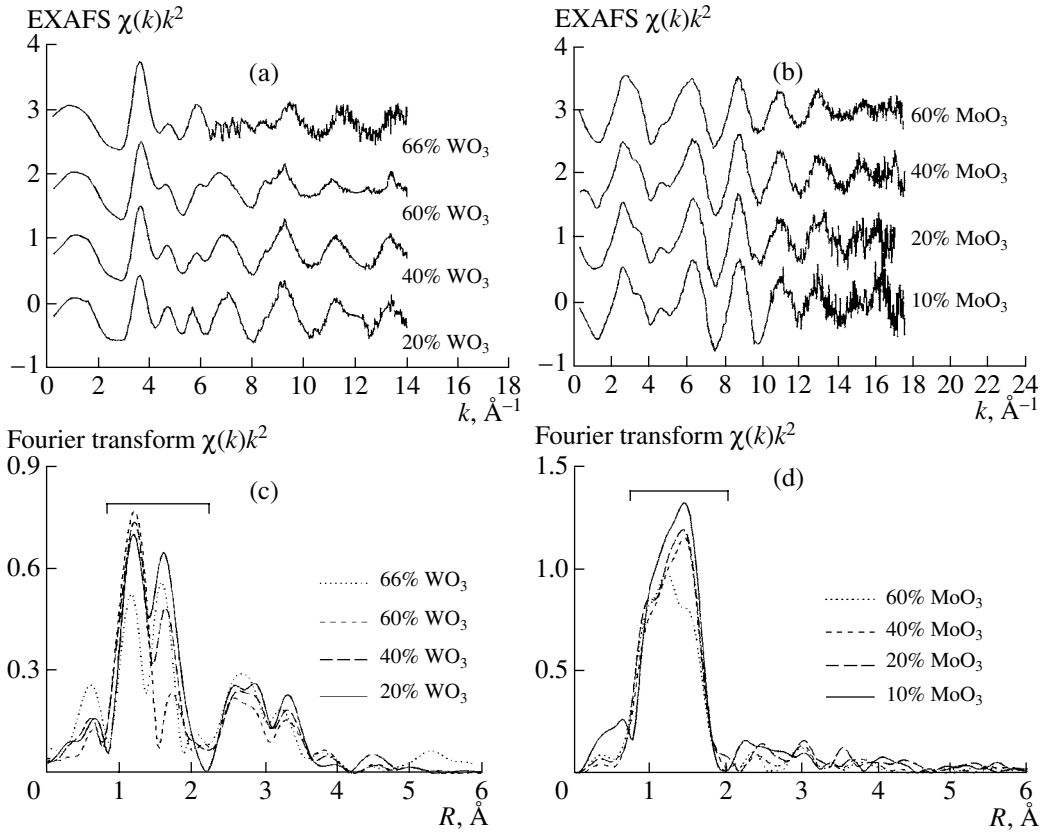

Fig. 28. (Top) EXAFS signals of the L_3 edge of tungsten and the K edge of molybdenum in barium tungsten phosphate glasses and calcium molybdenum phosphate glasses, respectively, and (bottom) their Fourier transforms. The region of the first coordination sphere is marked on the Fourier transforms.

Figure 28 shows some EXAFS components selected by the technique described above and their Fourier transforms. The first peak, located in the range from 0.8 to 2 Å, corresponds to the first coordination sphere. It makes the main contribution to the experimental EXAFS component, which manifests itself in the form of a dominant low-frequency signal. The peaks located at larger distances (>2 Å) are contributions from the many-particle distribution functions in the first coordination sphere and the subsequent coordination spheres. A large number of contributions and the strong overlap of their Fourier transforms make quantitative analysis impossible. Therefore, we will consider below only the contribution from the first coordination sphere of tungsten (molybdenum).

In description of the displacements of the metal atom from the octahedron center, we will use the following conditional designations: the directions corresponding to shifts to a vertex, edge, and the center of a face of the MeO_6 octahedron will be denoted as ⟨100⟩, ⟨110⟩, and ⟨111⟩, respectively (these designations are identical to the crystallographic directions for the cubic perovskite-type structure).

To obtain exact structural data, the EXAFS signal of the first coordination sphere was analyzed within the conventional multicomponent Gaussian model and by the model-independent method (see above). The radial distribution functions obtained are shown in Fig. 29. It can be seen well that the nearest oxygen atoms around the W atom in barium tungsten phosphate glasses are divided into two groups, three atoms in each (3 : 3 partition), which are located at distances of 1.7 and 2.0 Å (Fig. 29a). The wide peak located at a distance of 1.3 Å is a spurious (nonstructural) contribution and, apparently, is related to the oscillating component of the atomic absorption coefficient, the so-called atomic EXAFS signal (atomic XAFS [94]). The observed partition of the first coordination sphere of the tungsten atom corresponds to its displacement in the [111] direction to the octahedron face. With an increase in the content of tungsten oxide in a glass with 60% WO_3, the ratio of the intensities of the two peaks in the radial distribution function changes: the intensity of the peak located at a larger distance (2.0 Å) decreases. A possible reason for this effect is that some part of tungsten atoms begin to shift in the [110] direction. In this case, the first coordination sphere of tungsten is divided into two parts composed of four near and two far oxygen atoms (4 : 2 partition). Note that this distortion of the octahedron is similar to that observed in crystalline

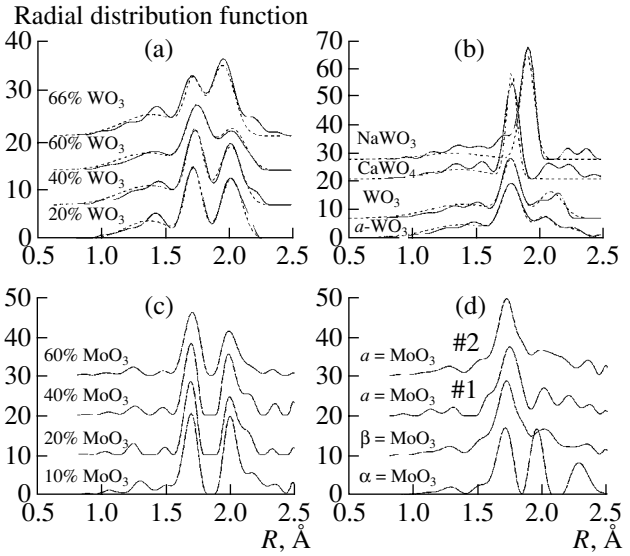

Fig. 29. Radial distribution functions for tungsten and molybdenum ions in $BaO–P_2O_5–WO_3$, $P_2O_5–WO_3$, and $CaO–P_2O_5–MoO_3$ glasses; thin amorphous films of *a*-WO_3 and *a*-MoO_3; and crystalline oxides $CaWO_4$, $NaWO_3$, *m*-WO_3, α-MoO_3, and β-MoO_3: calculation by the model-independent method (solid lines) and within the multicomponent Gaussian model (dashed lines).

WO_3. If we suggest that two types of centers are present in glass containing 60% WO_3, it follows from the ratio of the peak intensities in the radial distribution functions that the contents of [WO_6] octahedra with 3 : 3 and 4 : 2 distortions are about 70 and 30%, respectively (Table 2).

In a tungsten phosphate glass without barium oxide (66% WO_3), the first coordination sphere of tungsten is split into two parts composed of two and four oxygen atoms located at distances 1.7 and 2.0 Å, respectively. This distortion somewhat differs from that observed in glasses containing barium oxide and can be explained by the double role of tungsten oxide, which is involved in the glass network formation and, at the same time, acts as an oxide modifier.

Distortion of [WO_6] octahedra in an amorphous *a*-WO_3 film exceeds that in crystalline WO_3; however, these phases are similar in the type of partition of W–O bonds into groups. This similarity is in agreement with the nanocrystalline film structure. At the same time, the distortion in the *a*-WO_3 film significantly differs from that in glasses with a small content of tungsten oxide.

The distortion in calcium molybdenum phosphate glasses (Fig. 29c) is similar to that observed in barium tungsten phosphate glasses. Nevertheless, in this case, the first coordination sphere of molybdenum is distorted somewhat stronger, an effect that manifests itself in the asymmetric form of the far peak in the radial distribution function. Therefore, we can approximately assume that the local environment of molybdenum ions

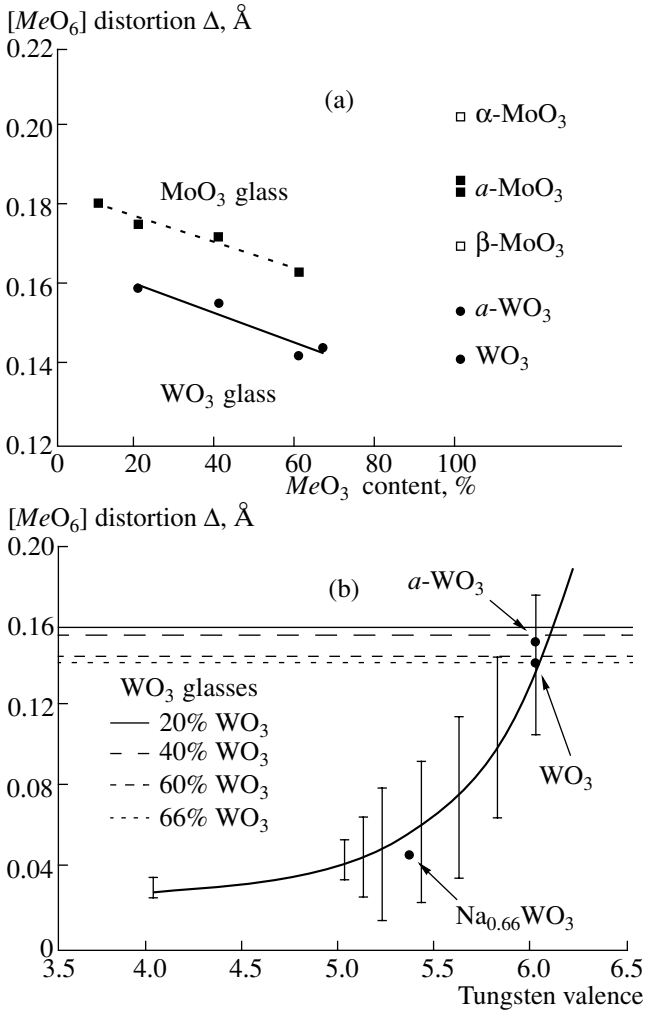

Fig. 30. Dependences of the distortion parameter Δ of the [MeO_6] octahedron (*Me* = W, Mo) on (a) the metal oxide content and (b) the valence state of tungsten.

is split into three groups: three oxygen atoms at a distance of 1.7 Å, two oxygen atoms at a distance of 2.0 Å, and one oxygen atom at a distance of 2.1 Å.

As in the case of tungsten phosphate glasses, the type of the distortion of the [MoO_6] octahedron in a glass differs from that in the crystalline α-MoO_3 and β-MoO_3 phases as well as in an amorphous *a*-MoO_3 film, in which molybdenum atoms are shifted from the center in the [110] direction. The type of distortion of the first coordination spheres of tungsten and molybdenum in glasses is the same as that found in monophosphate tungsten bronzes [94].

The degree of distortion of the [MeO_6] octahedron was quantitatively estimated by the formula $\Delta = \langle |R - \langle R \rangle| \rangle$ from the radial distribution functions. The results obtained are listed in Table 2. Figure 30b shows the dependence of the degree of octahedral distortion on the valence of tungsten ions [95]. The value of the distortion Δ found from the analysis of the EXAFS spectra

for crystalline and amorphous $W^{6+}O_3$ is in good agreement with the dependence observed. In the case of tungsten phosphate glasses, the calculated value of Δ suggests that most tungsten ions in glasses have a valence of 6+. In addition, a correlation was found between the degree of octahedral distortion and the percentage of metal oxide in the glass matrix (Fig. 30a). This circumstance indicates that distortion of the metal–oxygen octahedron is determined not only by the electronic structure of the metal ion but also by its interactions with the matrix material [89].

Thus, specific investigations of the structure of tungsten and molybdenum oxides show high efficiency of EXAFS spectroscopy based on synchrotron radiation beams in the study of the local electronic and atomic structures of absorbing centers.

6. INVESTIGATION OF STRUCTURAL FEATURES OF FULLERIDES

Investigations of metal-doped fullerites (fullerides) gave rise to a new field in physics. A number of A_xC_{60} phases (A = Na, K, Rb, Cs; x = 1, 2, 3, 4, 6) have been revealed. The study of physical properties of fullerene crystals is of particular interest in view of the observation of superconductivity in fullerite samples kept in potassium vapor (K_3C_{60}) at T_C = 10 K. This phenomenon is related to the intercalation of potassium atoms over interstitial positions in the fullerite lattice, in complete analogy with graphite. Further investigations with intercalants (alkali metals) of different types led to an increase in T_C from 10 K for Na_2CsC_{60} to 31 K for Rb_2CsC_{60}. The superconductivity in fullerene crystals is a very interesting and exotic phenomenon. Although the mechanism of this phenomenon is classical, there are certain specific features of the conduction band and vibrational modes.

There is another class of fullerides—AC_{60}—with stoichiometric phases, which exhibit a number of interesting properties. At high temperatures (above 380 K), AC_{60} crystallizes in the rock salt structure. Below 380 K, AC_{60} exists in two phases: a stable polymer orthorhombic (*Pnnm*) phase [96] and a metastable dimeric monoclinic ($P2_1/a$) phase [97].

The polymer phase, which consists of linear chains of C_{60} molecules, is formed upon slow cooling. This phase is stable and conducting. The dimeric phase is formed upon fast cooling of a sample from the high-temperature cubic phase and is nonconducting. The stable polymer phase has certain magnetic features and is unstable at low temperatures with respect to the generation of a spin (or charge) density wave. It was shown in [97] that some metastable phases (one of them has a primitive cubic structure with an unknown space group) are formed upon fast cooling to T = 150 K for CsC_{60} and 125 K for RbC_{60}.

Table 2. Distortion Δ (±0.001 Å) of the first coordination sphere of W (Mo) in glasses and crystals of tungsten and molybdenum oxides

Compound	Distortion type	Direction of displacement of the W (Mo) ion	Δ, Å
$CaWO_4$	4		0.045
$Na_{0.66}WO_3$	6		0.048
WO_3	4 : 2	[110]	0.143
a-WO_3	4 : 1 : 1	[110]	0.154
20% WO_3	3 : 3	[111]	0.160
40% WO_3	3 : 3	[111]	0.156
60% WO_3	3 : 3 (~70%)	[111]	0.143
	4 : 2 (~30%)	[110]	
66% WO_3	2 : 4		0.145
α-MoO_3	2 : 2 : 2	[110]	0.204
μ-MoO_3	4 : 2	[110]	0.171
a-MoO_3 #1	4 : 1 : 1	[110]	0.187
a-MoO_3 #2	4 : 1 : 1	[110]	0.184
10% MoO_3	3 : 2 : 1	[111]	0.181
20% MoO_3	3 : 2 : 1	[111]	0.176
40% MoO_3	3 : 2 : 1	[111]	0.172
60% MoO_3	3 : 2 : 1	[111]	0.164

Note: [110] and [111] are the directions of displacement from the octahedron center to the edge and face center, respectively.

The X-ray diffraction data obtained with the use of synchrotron radiation [96] clearly indicate that the twofold symmetry axis of the C_{60} molecule is directed along the crystallographic direction with the lattice parameter a = 9.13 Å. Another result is the observation of strong deformation of C_{60} molecules in the a direction, as a result of which a covalently bonded structure is formed. The specific π character of intermolecular bonds in polymer chains is consistent with the conclusion about the 1D-metallic character of this material.

Another important problem of structural analysis is the determination of the positions of metal atoms.

6.1. Subsystem of Alkali Metal Atoms

Let us consider structural changes in the subsystem of alkali metal atoms induced by a phase transition [98, 99].

According to the experimental data [96], the metal atom has an octahedral environment of C_{60} molecules (Fig. 31). A small radius of the alkali metal ion with respect to the sizes of the octahedron composed of large C_{60} molecules and strong anisotropy of the Debye–Waller factor for metal atoms suggest that the actual position of a metal atom differs from the central posi-

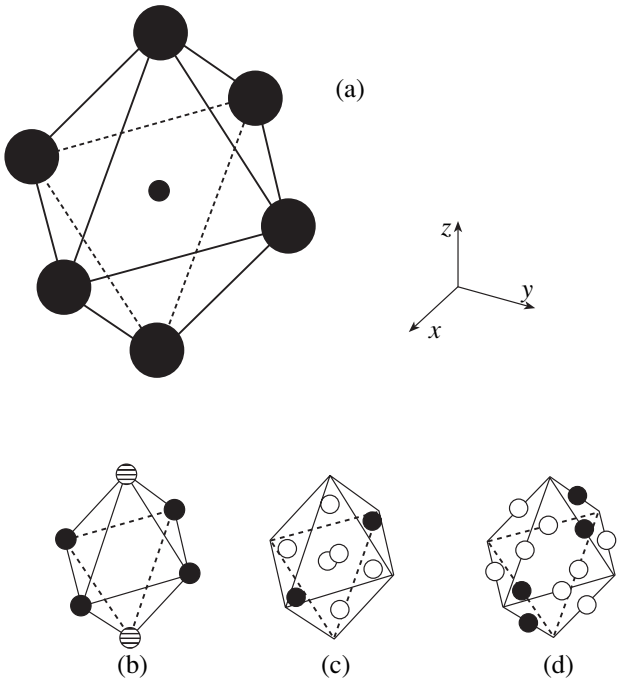

Fig. 31. Possible types of the metal atom positions (small circles) in the octahedral environment of the C_{60} molecule (large circles): (a) the central position 1*b* and (b–d) the 6*e*, 8*f*, and 12*i* positions, respectively.

tion shown in Fig. 31. Generally, according to [100], in the phase with rock salt structure, the following positions are possible for the octahedral environment: the central position **1*b*** with the coordinate (111) and local symmetry O_h; the sixfold position **6*e*** with the characteristic coordinate (00*z*) and the symmetry C_{4v}; and the positions **8*f*** ((*xxx*), C_{3v}), **12*i*** ((*xx*0), C_{2v}), **24*j*** ((*xy*0), C_s), and **24*k*** ((*xxz*), C_s).

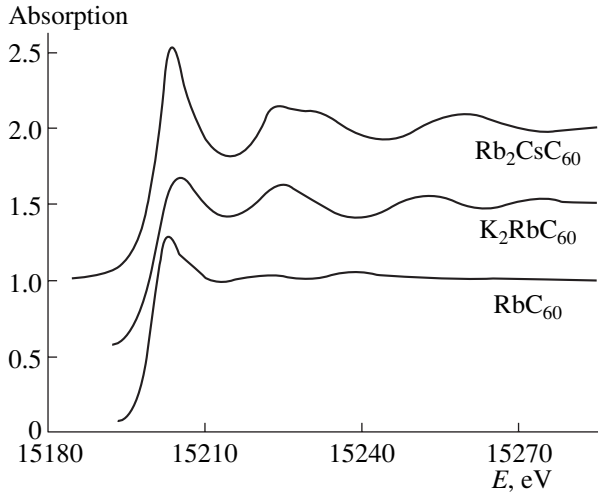

Fig. 32. Comparison of the Rb *K*-edge absorption spectra for RbC_{60} and the superconducting materials Rb_2CsC_{60} and K_2RbC_{60}.

In the **1*b*** position, a metal atom can vibrate only with respect to its equilibrium position. Such displacements with the wave vector $\mathbf{k} = 0$ are transformed according to the 3D irreducible representation F_{1u} and, therefore, cannot be related to the secondary order parameters of the E_g or F_{2g} symmetry. Similar displacements but with the wave vector (001) are transformed according to the irreducible representations τ_4 and τ_{10} and cannot be related to the order parameter $\xi_1 \neq 0$ of the τ_9 symmetry. Thus, a phase transition does not lead to any structural changes for a metal atom occupying the central position in the octahedron.

If a metal atom occupies an off-center position, a phase transition causes partial ordering over the positions shown in Figs. 31b–31d. For the **6*e*** position, the only secondary order parameter $\theta_2 \neq 0$ of the E_g symmetry describes the partial ordering of the metal atom either in the horizontal plane (filled circles) or over the two positions located above and below the plane (hatched circles). For the **8*f*** and **12*i*** positions (Figs. 31c, 31d), the secondary order parameters are $\eta_1 \neq 0, \xi_1 \neq 0$ and $\theta_2 \neq 0, \eta_1 \neq 0, \xi_1 \neq 0$, respectively. The occupied positions are shown as filled circles. The **24*j*** and **24*k*** positions originate from the **12*i*** and **8*f*** positions, respectively. The ordering of the metal atom over these positions is described by three secondary order parameters.

Therefore, we can suggest that complete ordering of metal atoms may occur with a further decrease in temperature and that the ordering phase transition leads to a lower symmetry, which is completely determined by the position type. For example, one of three possible versions of complete ordering of metal atoms for the positions **8*f*** with the wave vector $\mathbf{k} = 0$ leads to the space group C_{2v}^7.

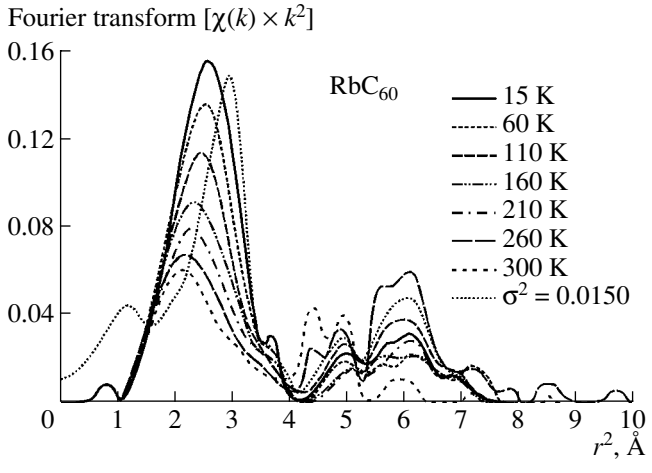

Fig. 33. Fourier transforms of EXAFS oscillations of Rb in comparison with the theoretical Fourier transforms for Rb in the central position.

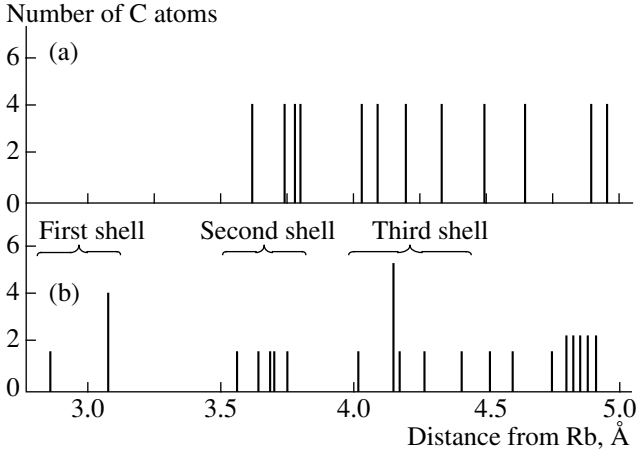

Fig. 34. Bar diagram of Rb–C distances: (a) Rb at the center of the octahedral interstitial site and (b) Rb in the off-center position (0.5, ε, ε), where ε = –0.07.

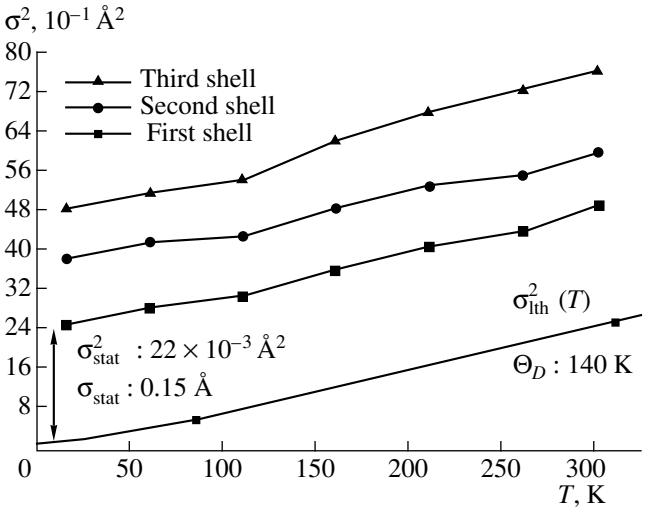

Fig. 35. Temperature dependences of squares of mean-square deviations σ^2_{123} of the radii of the nearest coordination spheres for Rb–C_{123}. Fitting of the $\sigma^2(T)$ data for the Debye model is shown.

6.2. EXAFS Investigation of the Orthorhombic Phase RbC_{60}

Let us consider the results of EXAFS study of the positions of metal atoms in the RbC_{60} compound [101]. These investigations were carried out to check the theoretical predictions reported in the previous section. The measurements were performed at the DESY synchrotron radiation source (Hamburg) [101]. A RbC_{60} fulleride sample had been previously classified by neutron and X-ray diffraction [102]. The lattice parameters were determined to be a = 14.262 Å, b = 9.109 Å, and c = 10.120 Å. We are interested in the exact position of Rb atoms in the structure. Possible off-center positions in this phase were noted in the X-ray diffraction study [102]. In the corresponding cubic and superconducting A_3C_{60} and A_2BC_{60} systems, where A = K or Rb and B = Rb or Cs, systematic EXAFS study has revealed off-center positions of A and B ions in the octahedral position [103].

The experiments were performed with the use of the ROMO II synchrotron radiation beam in the temperature range from 15 to 300 K. Figure 32 shows a typical Rb K-edge absorption spectrum for the orthorhombic phase RbC_{60} in comparison with Rb_2CsC_{60}, where Rb occupies only the tetrahedral (***T***) interstitial sites, and K_2RbC_{60}, where Rb occupies octahedral (***O***) interstitial sites. Both the near-edge structure and weak EXAFS oscillations indicate an Rb position with low local symmetry for RbC_{60}; the distribution of the nearest carbon atoms is similar to that for the Rb position in K_2RbC_{60} [17]. Figure 33 shows the Fourier transform of Rb EXAFS oscillations at different temperatures and the calculated Fourier transforms with the Rb–C distances obtained for the central Rb position in the O site with the use of theoretical values of the scattering amplitudes and phase shifts [17]. These Rb–C distances are shown in Fig. 34 in the form of a bar diagram. There is a clear difference between the experimental and theoretical data at the maximum of the radial distribution function, a result that resembles the situation in the analysis of O sites in [17]. A reasonable fitting of the measured Fourier transform spectra was obtained with the use of the off-center position (0.5, ε, ε), where ε = –0.07, and with the distribution of Rb–C distances that is shown in Fig. 34b.

In the preliminary EXAFS analysis, inversely transformed spectra were fitted with the use of three coordination spheres of carbon. The distributions of Rb–C distances obtained by this procedure are shown in Fig. 34b. A good fitting was obtained with the following values: $Rb–C_1$ = 3.08(2) Å, $Rb–C_2$ = 3.54(3) Å, and $Rb–C_3$ = 3.90(5)Å. These distances are almost temperature-independent. In the second stage of the analysis, we fixed these values for the distances and determined their squared deviations. The mean-square deviations $\sigma^2(T)$ of the Rb–C distances are shown in Fig. 35: the fitted value of the Debye temperature of 140 K in the EXAFS method for the first coordination sphere well describes the strong temperature dependence of the EXAFS signal (Fig. 33). Relatively large static contributions $\sigma^2(T)$ reflect the distribution of Rb–C distances that is shown in Fig. 34.

CONCLUSIONS

With the development of synchrotron radiation sources, EXAFS spectroscopy has become one of the main methods in the study of structures of amorphous and quasicrystalline media of various origin. This method is very promising for study of nanostructured

systems, such as quantum dots, nanotubes, fine-grained semiconductor structures, and nanomaterials for fabrication of new medicinal products.

REFERENCES

1. http://www.esrf.fr/.
2. H. Fricke, Phys. Rev. **16**, 202 (1920).
3. G. Hertz, Z. Phys. **3**, 19 (1920).
4. D. Coster, Z. Phys. **25**, 83 (1924).
5. A. E. Lindh, Z. Phys. **6**, 303 (1921); **31**, 210 (1925).
6. B. B. Ray, Z. Phys. **55**, 119 (1929).
7. B. Kievit and G. A. Lindsay, Phys. Rev. **36**, 648 (1930).
8. J. D. Hanawalt, Z. Phys. **70**, 20 (1931); Phys. Rev. **37**, 715 (1931).
9. R. de L. Kronig, Z. Phys. **70**, 317 (1931).
10. R. de L. Kronig, Z. Phys. **75**, 468 (1932).
11. H. Peterson, Z. Phys. **76**, 768 (1932); **80**, 528 (1933); **98**, 569 (1936).
12. A. I. Kostarev, Zh. Éksp. Teor. Fiz. **11**, 60 (1941); **19**, 413 (1949).
13. M. Sawada, Annu. Rep. Sci. Works, Fac. Sci., Osaka Univ. **7**, 1 (1959).
14. V. V. Shmidt, Izv. Akad. Nauk SSSR, Ser. Fiz. **25**, 977 (1961); **27**, 392 (1963).
15. A. I. Kozlenkov, Izv. Akad. Nauk SSSR, Ser. Fiz. **25**, 957 (1961); **27**, 364 (1963); **38**, 500 (1974).
16. D. E. Sayers, E. A. Stern, and W. F. Lytle, Phys. Rev. Lett. **27**, 1024 (1971).
17. T. Thole, P. Carra, F. Sette, and G. van der Laan, Phys. Rev. Lett. **8**, 1943 (1992).
18. C. T. Chen, F. Sette, Y. Ma, and S. Modesty, Phys. Rev. B **42**, 7262 (1990).
19. E. Dartyge, C. Depautex, Y. M. Dubuisson, et al., Nucl. Instrum. Methods Phys. Res., Sect. A **246**, 452 (1986).
20. C. Kunz, in *Synchrotron Radiation Techniques and Applications*, Ed. by C. Kunz (Springer-Verlag, Berlin, 1979).
21. B. M. Kincaid and P. Eisenberg, Phys. Rev. Lett. **34**, 1361 (1975).
22. *X-ray Data Booklet*, Ed. by V. Douglas (Univ. of California Press, Berkeley, 1986).
23. *Synchrotron Radiation Sources and Applications: Proceedings of the Thirtieth Scottish Universities Summer School in Physics, Aberdeen, 1985,* Ed. by G. N. Greaves (The Scottish Universities Summer School in Physics, Edinburgh, 1989).
24. *Synchrotron Radiation Research*, Ed. by H. Winick (Plenum, New York, 1980).
25. A. Fontane, in *Proceedings of the School of the Use of Synchrotron Radiation in Science and Technology, Miramare Trieste, Italy, 1997.*
26. V. Efimov, E. Efimova, S. Tyutyunnikov, et al., Poverkhnost, No. 6, 23 (2006).
27. A. Kuzmin, N. Mironova, J. Purans, and A. Radionov, J. Phys.: Condens. Matter **7**, 9357 (1995).
28. A. Kuzmin, J. Purans, G. Dalba, et al., J. Phys.: Condens. Matter **7**, 9083 (1996).
29. B. K. Teo, *EXAFS: Basic Principles and Data Analysis* (Springer-Verlag, Berlin, 1986).
30. *X-ray Absorption: Principles, Applications, Techniques of EXAFS, SEXAFS, and XANES*, Ed. by D. C. Koningsberger and R. Prins (Wiley, New York, 1988).
31. D. I. Kochubeĭ, Yu. A. Babanov, K. I. Zamaraev, et al., *X-ray Spectral Method for Studying the Structure of Amorphous Solids: EXAFS Spectroscopy* (Nauka, Novosibirsk, 1988) [in Russian].
32. A. Kuzmin, Physica B **208–209**, 175 (1995).
33. A. Kuzmin, J. Phys. (Paris) **7**, 2 (1997).
34. A. Kuzmin, EDA: EXAFS Data Analysis Software Package. User's Manual. Version 5.1 (Riga, 1999) (http://www.dragon.lv/eda).
35. R. V. Vedrinskiĭ and I. I. Geguzin, *X-ray Absorption Spectra of Solids* (Énergoatomizdat, Moscow, 1991) [in Russian].
36. S. J. Gurman, N. Binsted, and I. Ross, J. Phys. C: Solid State Phys. **17**, 143 (1984).
37. N. Binsted and S. S. Hasnain, J. Synchrotron. Radiat. **3**, 185 (1996).
38. J. J. Rehr, J. Mustre de Leon, S. I. Zabinsky, and R. C. Albers, J. Am. Chem. Soc. **113**, 5135 (1991).
39. J. J. Rehr, S. I. Zabinsky, and R. C. Albers, Phys. Rev. Lett. **69**, 3397 (1992).
40. S. I. Zabinsky, J. J. Rehr, A. Ankudinov, et al. Phys. Rev. B: Condens. Matter Mater. Phys. **52**, 2995 (1995).
41. A. L. Ankudinov, B. Ravel, J. J. Rehr, and S. D. Conradson, Phys. Rev. B: Condens. Matter Mater. Phys. **58**, 7565 (1998).
42. A. Filipponi, A. Di Cicco, T. A. Tyson, and C. R. Natoli, Solid State Commun. **78**, 265 (1991).
43. A. Filipponi, A. Di Cicco, and C. R. Natoli, Phys. Rev. B: Condens. Matter Mater. Phys. **52**, 15122 (1995).
44. A. Filipponi and A. Di Cicco, Phys. Rev. B: Condens. Matter Mater. Phys. **52**, 15135 (1995).
45. A. Di Cicco, M. J. Rosolen, R. Marassi, et al., J. Phys.: Condens. Matter **8**, 10779 (1996).
46. A. Kuzmin, J. Purans, M. Benfatto, and C. R. Natoli, Phys. Rev. B: Condens. Matter Mater. Phys. **47**, 2480 (1993).
47. A. Kuzmin and R. Grisenti, Philos. Mag. B **70**, 1161 (1994).
48. A. Kuzmin and J. Purans, J. Phys.: Condensed Matter **5**, 267 (1993).
49. J. Purans, A. Kuzmin, Ph. Parent, and H. Dexpert, Physica B **208–209**, 373 (1995).
50. G. Dalba, D. Diop, P. Fornasini, et al., J. Phys.: Condensed Matter **5**, 1643 (1993).
51. A. Kuzmin, S. Obst, and J. Purans, J. Phys.: Condensed Matter **9**, 10065 (1997).
52. A. Kuzmin and J. Purans, J. Phys.: Condensed Matter **5**, 9423 (1993).
53. A. Kuzmin and Ph. Parent, J. Phys.: Condensed Matter **6**, 4395 (1994).
54. A. Kuzmin, J. Purans, and Ph. Parent, Physica B **208–209**, 45 (1995).
55. J. Purans, A. Kuzmin, Ph. Parent, and C. Laffon, Ionics **4**, 101 (1998).

56. A. Kuzmin and J. Purans, Proc. SPIE **2968**, 180 (1997).
57. A. Kuzmin and J. Purans, J. Phys.: Condensed Matter **5**, 2333 (1993).
58. E. Burattini, J. Purans, and A. Kuzmin, Jpn. J. Appl. Phys. **32** (Suppl. 32-2), 655 (1993).
59. A. Balerna, E. Bernieri, E. Burattini, et al., Nucl. Instrum. Methods Phys. Res., Sect. A **308**, 234 (1991).
60. E. A. Stern, Phys. Rev. B: Solid State **10**, 3027 (1974).
61. A. Filipponi and A. Di Cicco, Phys. Rev. B: Condens. Matter Mater. Phys. **51**, 12322 (1995).
62. G. Bunker, Nucl. Instrum. Methods Phys. Res., Sect. A **207**, 437 (1983).
63. J. M. Tranquada and R. Ingalls, Phys. Rev. B: Condens. Matter Mater. Phys. **28**, 3520 (1983).
64. G. Dalba, P. Fornasini, and F. Rocca, Phys. Rev. B: Condens. Matter Mater. Phys. **47**, 8502 (1993).
65. Yu. A. Babanov, V. V. Vasin, A. L. Ageev, and N. V. Ershov, Phys. Status Solidi B **105**, 747 (1981).
66. N. V. Ershov, A. L. Ageev, V. V. Vasin, and Yu. A. Babanov, Phys. Status Solidi B **108**, 103 (1981).
67. D. S. Yang and G. Bunker, Phys. Rev. B: Condens. Matter Mater. Phys. **54**, 3169 (1996).
68. P. Kizler, in *Proceedings of the 6th International Conference on X-ray Absorption Fine Structure, York*, Ed. by S. S. Hasnain (Ellis Horwood, Singapore, 1991), p. 78.
69. S. J. Gurman and R. L. McGreevy, J. Phys.: Condens. Matter **2**, 9463 (1990).
70. C. E. Bouldin and E. A. Stern, in *EXAFS Studies of Amorphous Semiconductors, EXAFS and Near Edge Structure III*, Ed. by K. O. Hodgson, B. Hedman, and J. E. Penner-Hahn (Springer-Verlag, Berlin, 1984), p. 273.
71. E. A. Stern, Y. Ma, O. Hanske-Petitpierre, and C. E. Bouldin, Phys. Rev. B: Condens. Matter Mater. Phys. **46**, 687 (1992).
72. B. K. Teo and P. A. Lee, J. Am. Chem. Soc. **101**, 2815 (1979).
73. A. G. McKale, B. W. Veal, A. P. Paulikas, et al., J. Am. Chem. Soc. **110**, 3763 (1988).
74. M. F. Ruiz-Lopez, M. Loos, J. Goulon, et al., Chem. Phys. **121**, 419 (1988).
75. M. F. Ruiz-Löpez, F. Bohr, A. Filipponi, et al., in *Proceedings of the 6th International Conference on X-ray Absorption Fine Structure, York*, Ed. by S. S. Hasnain (Ellis Horwood, Singapore, 1991), p. 75.
76. T. A. Tyson, PhD. Thesis (Stanford University, 1991).
77. G. Dalba, P. Fornasini, A. Kuzmin, et al., J. Phys.: Condens. Matter **7**, 1199 (1995).
78. E. A. Stern, in *X-ray Absorption: Principles, Applications, Techniques of EXAFS, SEXAFS, and XANES*, Ed. by D. C. Koningsberger and R. Prins (Wiley, New York, 1988), p. 3.
79. A. Filipponi, A. Di Cicco, M. Benfatto, and C. R. Natoli, Europhys. Lett. **13**, 319 (1990).
80. E. I. Pustyl'nik, *Statistical Methods of Analysis and Treatment of Observations* (Nauka, Moscow, 1968) [in Russian].
81. B. Tolentino, E. Darty, A. Fontone, et al., J. Appl. Crystallogr. **21**, 15 (1988).
82. R. Clarke, Nucl. Instrum. Methods Phys. Res., Sect. A **291**, 117 (1990).
83. V. L. Aksenov, I. N. Ivanov, et al., Preprint No. C14-96-502, OIYaI (Joint Institute for Nucleus Research, Dubna, 1996).
84. D. Andrault, U. J. Peryronnea, F. Farget, and J. P. Itie, Physica B **208–209**, 327 (1995).
85. K. Zhang, J. Dong, and D. S. Auld, Physica B **208–209**, 719 (1995).
86. U. Hatje, M. Hagelstein, T. Refler, and H. Forster, Physica B **208–209**, 646 (1995).
87. M. Kovalenko, V. Mironov, V. Shaliapin, and S. Tiutiunnikov, J. Alloys Compd. **286**, 26 (1999).
88. C. G. Granqvist, *Handbook on Inorganic Electrochromic Materials* (Elsevier Science, Amsterdam, 1995).
89. M. Kunz and I. D. Brown, J. Solid State Chem. **115**, 395 (1995).
90. I. B. Bersuker, *Electronic Structure and Properties of Coordination Compounds*, 3rd ed. (Khimiya, Leningrad, 1986) [in Russian].
91. A. Kuzmin and J. Purans, J. Phys. (Paris) **7**, 2-971 (1997).
92. A. Kuzmin and J. Purans, Proc. SPIE **2968**, 180 (1997).
93. J. J. Rehr, S. I. Zabinsky, A. Ankudinov, and R. C. Albers, Physica B **208–209**, 23 (1995).
94. P. Labbe, M. Goreaud, and B. Raveau, J. Solid State Chem. **61**, 324 (1986).
95. B. Domengés, N. K. McGuire, and M. O'Keeffe, J. Solid State Chem. **56**, 94 (1985).
96. P. W. Stephens, G. Bortel, G. Faigel, et al., Nature **370**, 636 (1994).
97. G. Oszlanyi, G. Bortel, G. Faigel, et al., Phys. Rev. B: Condens. Matter Mater. Phys. **54**, 11849 (1996).
98. V. L. Aksenov, Yu. A. Osipyan, and V. S. Shakhmatov, Pis'ma Zh. Éksp. Teor. Fiz. **62** (1), 428 (1995) [JETP Lett. **62**, 417 (1995)].
99. V. L. Aksenov, Yu. A. Osipyan, and V. S. Shakhmatov, J. Low Temp. Phys. **107**, 547 (1997).
100. O. V. Kovalev, *Irreducible and Induced Representations and Corepresentations of Fedorov Groups* (Nauka, Moscow, 1986) [in Russian].
101. V. L. Aksenov, H. Gieters, Yu. S. Grushko, et al., DESY Annual Report (Hamburg, 1998).
102. P. Launois, Phys. Rev. Lett. **81**, 4420 (1998).
103. G. Nowitzke, G. Wortmann, H. Werner, et al., Phys. Rev. B: Condens. Matter Mater. Phys. **54**, 13230 (1996); Mol. Cryst. Liq. Cryst. **245**, 321 (1994).

Translated by Yu. Sin'kov